

Cell-intrinsic metabolic phenotypes identified in patients with glioblastoma, using mass spectrometry imaging of ¹³C-labelled glucose metabolism

Received: 28 May 2024

Accepted: 27 March 2025

Published online: 19 May 2025

 Check for updates

Anastasia Tsyben¹, Andreas Dannhorn², Gregory Hamm²,
Manthos Pitoulias¹, Dominique-Laurent Couturier¹, Ashley Sawle¹,
Mayen Briggs¹, Alan J. Wright¹, Cara Brodie¹, Lee Mendil¹, Jodi L. Miller¹,
Eleanor C. Williams^{3,4}, Lovisa Franzén^{5,6}, Grand De Jong⁷, Tannia Gracia⁷,
Fani Memi⁷, Omer Ali Bayraktar⁷, Ram Adapa¹, Jyotsna Rao¹,
Ariadna González-Fernández⁸, CRUK Rosetta Grand Challenge Consortium*,
Josephine Bunch^{8,9}, Zoltan Takats⁹, Simon T. Barry³,
Richard J. A. Goodwin², Richard Mair^{1,10}✉ & Kevin M. Brindle^{1,11}✉

Transcriptomic studies have attempted to classify glioblastoma (GB) into subtypes that predict survival and have different therapeutic vulnerabilities^{1–3}. Here we identified three metabolic subtypes: glycolytic, oxidative and a mix of glycolytic and oxidative, using mass spectrometry imaging of rapidly excised tumour sections from two patients with GB who were infused with [U-¹³C]glucose and from spatial transcriptomic analysis of contiguous sections. The phenotypes are not correlated with microenvironmental features, including proliferation rate, immune cell infiltration and vascularization, are retained when patient-derived cells are grown in vitro or as orthotopically implanted xenografts and are robust to changes in oxygen concentration, demonstrating their cell-intrinsic nature. The spatial extent of the regions occupied by cells displaying these distinct metabolic phenotypes is large enough to be detected using clinically applicable metabolic imaging techniques. A limitation of the study is that it is based on only two patient tumours, albeit on multiple sections, and therefore represents a proof-of-concept study.

GB is the most common primary adult brain cancer⁴. Transcriptomic analyses have attempted to classify GB into subtypes that could predict treatment response^{1–3}, and a recent study that used a pathway-based classification defined metabolism-associated subtypes with distinct therapeutic vulnerabilities. These included a mitochondrial subtype, which is associated with a more favourable clinical outcome and is sensitive to inhibitors of oxidative phosphorylation, and a glycolytic, plurimetabolic subtype that is resistant to multiple treatment types⁵.

An important question is the extent to which the metabolism displayed by tumour cells in vivo is cell-intrinsic and how much is defined by the tumour microenvironment (TME)⁶. We addressed this question by using mass spectrometry imaging (MSI) of rapidly excised tumour sections from patients with GB who were infused with [U-¹³C] glucose immediately before surgery to image tumour cell metabolic activity in vivo and from a spatial transcriptomic analysis of adjacent sections.

A full list of affiliations appears at the end of the paper. ✉ e-mail: Richard.Mair@cruk.cam.ac.uk; kmb1001@cam.ac.uk

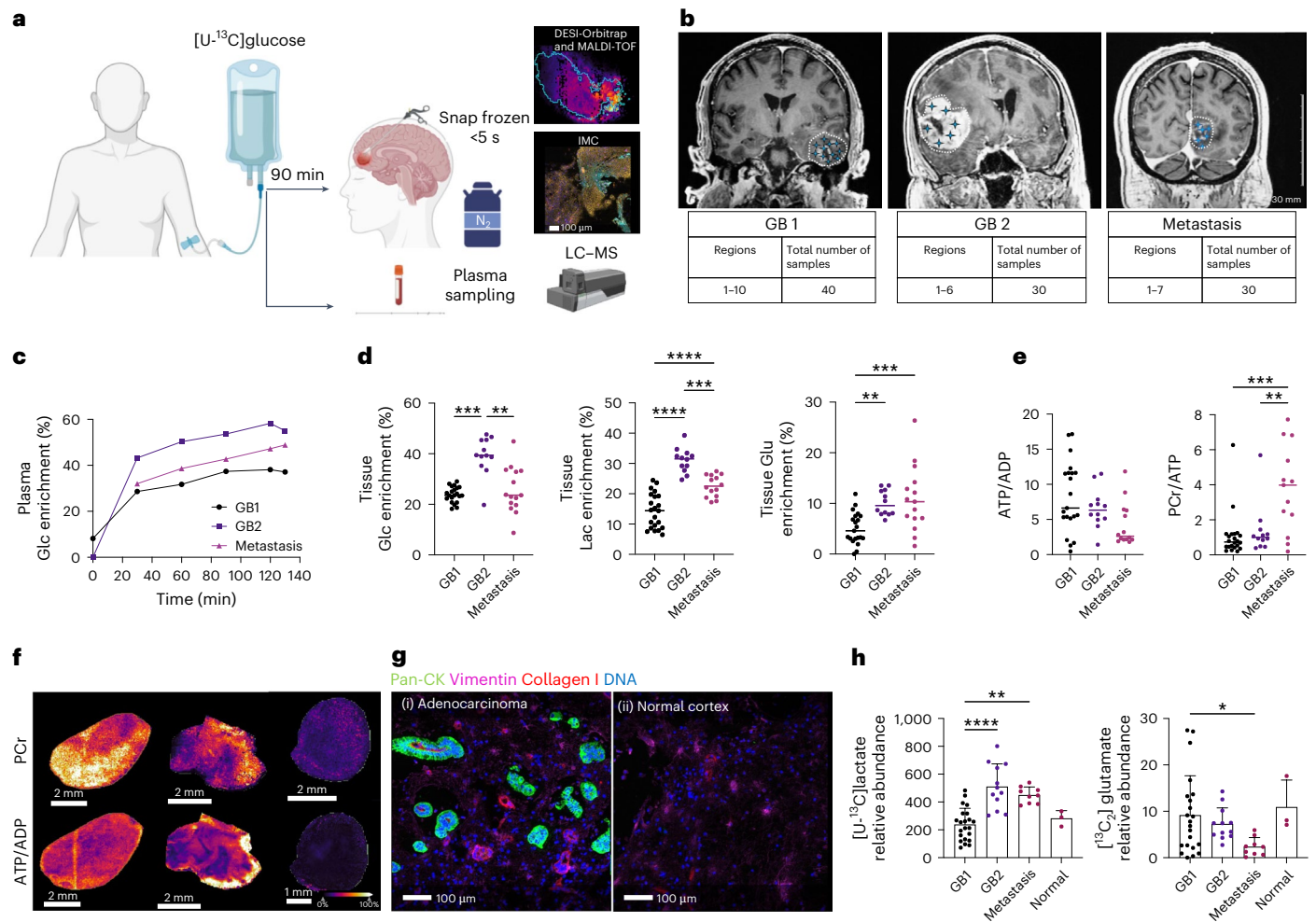


Fig. 1 | Intra-operative freezing rapidly arrests tissue metabolism and allows visualisation of metabolic activity. a, Patients were infused intra-operatively with [U-¹³C]glucose and underwent multi-regional tumour sampling followed by rapid freezing in liquid nitrogen (<5 s). Tumour sections (10 μm) were analysed using DESI-MSI and MALDI-MSI, and contiguous sections were analysed by IMC. Blood samples were collected before, during and after infusion for plasma liquid chromatography–MS (LC–MS) analysis. Created in BioRender.com.

b, Coronal MR images from the three patients who were infused, showing the locations of the sampled regions (blue stars). The number of regions sampled is shown for each patient; each region had three to six pieces of snap-frozen tissue. **c**, Plasma glucose (Glc) fractional labelling in the three infused patients. Tumour sampling commenced at 90 min. **d**, Glucose and metabolite fractional labelling in the tumour tissue: Glc ([U-¹³C]glucose/([U-¹³C]glucose + [U-¹²C]glucose) (GB1 vs GB2, $P = 0.0001$; GB2 vs Metastasis, $P = 0.004$); lactate (Lac) ([U-¹³C]lactate/([U-¹³C]lactate + [U-¹²C]lactate) (GB1 vs GB2, $P < 0.0001$; GB2 vs Metastasis, $P = 0.0002$; GB1 vs Metastasis, $P < 0.0001$); and glutamate (Glu) ([¹³C₂]glutamate/([¹³C₂]glutamate + [U-¹²C]glutamate) (GB1 vs GB2, $P = 0.0069$;

GB1 vs Metastasis, $P = 0.0008$). **e**, ATP/ADP and PCR signal intensity ratios in each tumour section (PCR/ATP GB1 vs Metastasis, $P = 0.0001$; GB2 vs Metastasis, $P = 0.0033$). **f**, Representative tumour sections from each patient showing PCR signal intensities and ATP/ADP signal intensity ratios. **g**, Representative sections from the metastasis and from normal-appearing brain (data reproduced in three additional sections of normal cortex and nine of the metastasis); (i) Pan-cytokeratin (CK)-positive (green) adenocarcinoma cells formed tubules around a central Collagen I-positive vessel (red). The tubules are surrounded by vimentin-positive (pink) cortex. (ii) Normal-appearing cortical tissue was obtained from the margin of the metastasis and showed vimentin-positive cells and an absence of adenocarcinoma cells. **h**, Relative abundance of [U-¹³C]lactate (GB1 vs GB2, $P < 0.0001$; GB1 vs Metastasis, $P = 0.0016$) and [¹³C₂]glutamate (GB1 vs Metastasis, $P = 0.0394$) in tumour sections from GB1 ($n = 22$), GB2 ($n = 12$), the adenocarcinoma metastasis ($n = 9$) and normal-appearing cortex ($n = 3$). Data are means; error bars, s.d.; every dot is a tissue section. Asterisks refer to P values obtained from a one-way ANOVA followed by Tukey's multiple comparisons test ($*P < 0.05$, $**P < 0.005$, $***P < 0.0005$, $****P < 0.00005$).

Results

We infused three patients, two with GB and a third with an adenocarcinoma metastasis, with [U-¹³C]glucose and performed MSI on rapidly excised tumour tissue that was dissected during tumour debulking surgery (Fig. 1a). We sampled 16 regions from two patients with GB and seven regions from the patient with a metastasis, the latter containing samples from normal-appearing cortex (Fig. 1b). There were no significant differences in lactate and glutamate ¹³C labelling between the tumour mass and tumour margin (Extended Data Fig. 1a).

Tissue sampling began 90 min after the start of infusion⁷, during which time the plasma glucose fractional enrichment reached a

steady state (Fig. 1c). Fractional labelling of lactate, an end product of the glycolytic pathway, and of [¹³C₂]glutamate, which is labelled via α-ketoglutarate in the tricarboxylic acid (TCA) cycle (Extended Data Fig. 1b) in GB1 and GB2, were less than that of tumour glucose (Fig. 1d), suggesting that neither had reached isotopic steady state and were therefore a measure of glycolytic and TCA cycle activity, respectively. There was a direct correlation between [¹³C₂]glutamate signal intensities and the intensities of the TCA cycle intermediates [¹³C₂]malate, [¹³C₂]fumarate and [¹³C₂]succinate (Extended Data Fig. 1c). The signal from ceramide-1-phosphate (752.596 m/z) confirmed minimal variation in instrument performance during acquisition and uniformity of tissue preparation (Extended Data Fig. 1d). Mass errors on the metabolite

ions and the mass isotopologue distributions of all detectable labelled metabolites are given in Supplementary Tables 1 and 2, respectively. The sampling technique rapidly arrested tissue metabolism, as indicated by the ATP/ADP and phosphocreatine PCr/ATP ratios (Fig. 1e,f), which decline rapidly in hypoxic or ischaemic brain tissue⁸. Preservation of the ATP, ADP and PCr concentrations was also demonstrated using ³¹P nuclear magnetic resonance (NMR) measurements (Extended Data Fig. 2a,b). The metabolite ¹³C labelling observed was assumed, therefore, to be similar to that present in vivo. The ATP and PCr signal intensities were similar in the two GB tumours but significantly higher than those in the metastasis (Extended Data Fig. 2c). The concentrations of plasma amino acids and lactate did not change significantly during the infusion protocol. The plasma concentrations of ¹³C-labelled lactate and glutamine, although less than 10% of the unlabelled concentrations, could have contributed to some of the labelled lactate and, via glutamine, the labelled glutamate observed in the tumour sections (Extended Data Fig. 2d and Supplementary Table 3).

Metabolic profiles of normal cortex and GB tumours

The metastatic adenocarcinoma occupied small, discrete areas surrounded by gliotic and normal-appearing brain parenchyma (Fig. 1g) and therefore provided apparently normal brain tissue for comparative analysis. We segmented the mass spectrometry (MS) images using seven ¹³C-labelled metabolites from glycolysis ([U-¹³C]pyruvate, [U-¹³C]lactate) and the TCA cycle ([¹³C₂]fumarate, [¹³C₂]succinate, [¹³C₂]malate, [¹³C₂]glutamate and [¹³C₂]glutamine). This separated the tumour, gliotic and normal-appearing brain parenchyma and agreed with tissue classification performed by a histopathologist (Extended Data Fig. 2e).

Next, we assessed glycolytic activity and TCA cycle activity in the tumours and in normal-appearing brain. [U-¹³C]lactate signals were significantly lower in GB1 than in GB2 and the metastasis, whereas the [¹³C₂]glutamate signals in GB1 were significantly higher than in the metastasis (Fig. 1h), reflecting higher glycolytic and lower TCA cycle activities in the metastasis. Glutamate labelling in the GB tumours was comparable to that in normal brain.

Metabolite ¹³C-labelling identifies GB metabolic phenotypes

We segmented the GB MS images using the same seven ¹³C-labelled metabolites from glycolysis and the TCA cycle. We reasoned that the activity of these two pathways could result in four cellular states; however, the MSI spectra did not contain a high glycolytic, high TCA cycle phenotype, and images were better segmented assuming only three metabolic states (Fig. 2a and Extended Data Fig. 3a): state 3 (high glycolysis, low TCA cycle), state 2 (low glycolysis, high TCA cycle) and state 1 (low activity in both pathways). Segmentation assuming three

or four metabolic states showed that these states occupied distinct and spatially extensive regions (Fig. 2b and Extended Data Fig. 3b–e). As observed previously from transcriptomic data⁵, each tumour had a predominant metabolic phenotype, with GB1 containing more of state 2 and GB2 containing more of state 3 (Extended Data Fig. 3f). Nevertheless, regions occupied by one of these three metabolic states co-existed in both tumours, sometimes within a single tumour section. Spatial RNA sequencing of adjacent tumour sections and segmentation using Hallmark oxidative and glycolytic gene sets also found three metabolic states: glycolytic, oxidative and mixed (Extended Data Fig. 4a), which showed a strong correlation with the MSI data (Fig. 2c) and an overall concordance of 65% (Extended Data Fig. 4b).

Metabolic phenotypes do not correlate with microenvironment

To exclude perfusion and hypoxia as explanations for the observed metabolic heterogeneity, we assessed cellular energy status from measurements of the ATP, ADP and PCr concentrations. All tumour regions had ATP/ADP and PCr/ATP ratios comparable to those in normal brain (Fig. 2d). ADP was more abundant in the more oxidative tumour regions (Extended Data Fig. 4c), consistent with a high intramitochondrial ADP concentration⁹.

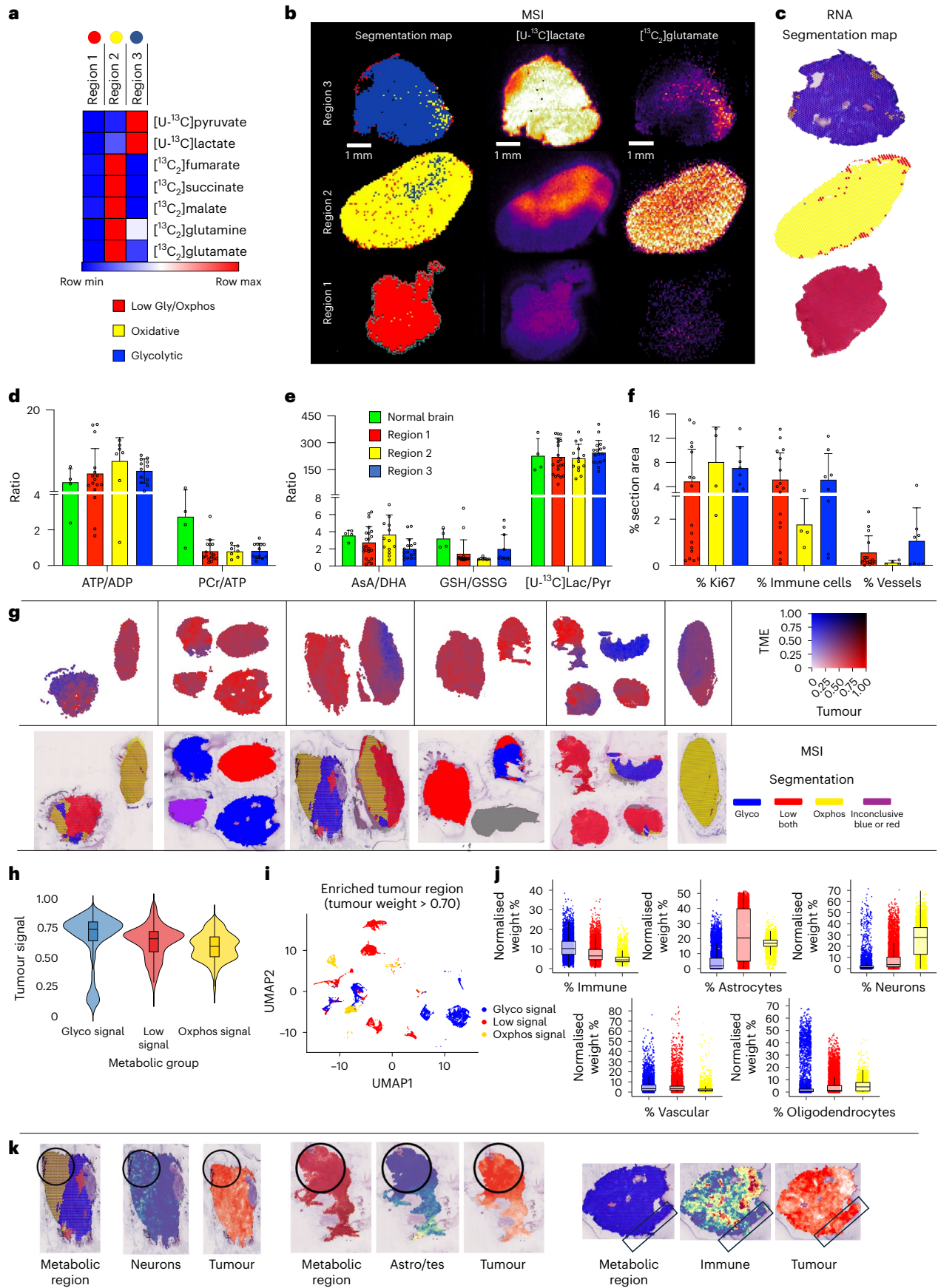
The three metabolic states and normal brain showed similar redox status, as assessed from measurements of the ascorbic acid to dehydroascorbic acid (AsA:DHA) and reduced to oxidized glutathione (GSH:GSSG) ratios, reflecting the NADPH/NADP⁺ ratio¹⁰, and the [U-¹³C]lactate/[U-¹³C]pyruvate ratios, reflecting the NADH/NAD⁺ ratio¹¹ (Fig. 2e).

Next, we analysed contiguous sections by imaging mass cytometry (IMC) for the presence of immune cells, blood vessels and proliferating cells. We defined five immune phenotypes: CD3⁺CD45⁺CD4⁺ (helper T cells)¹²; CD3⁺CD45⁺CD8⁺ (cytotoxic T cells)¹³; CD3⁺CD45⁺CD8⁺GZMB⁺ (activated T cells)¹⁴; CD45⁺GZMB⁺ (natural killer or neutrophils)¹⁵; and CD68⁺ (macrophages or microglia)¹⁶. Vascular phenotypes included large vessels (ASMA⁺CollagenI⁺panCK⁺CD31⁺)¹⁷ and small vessels or capillaries (CD31⁺CollagenI⁺)¹⁸. Regions occupied by the different metabolic states showed similar numbers of Ki67⁺ cells, immune cell phenotypes and blood vessels (Fig. 2f and Extended Data Fig. 5a,b), with the only significant difference being slightly fewer CD68⁺ cells in the oxidative regions. However, the proportion of immune cells was small, representing less than 10% of the total cell population. Cell density could also not account for the observed metabolic heterogeneity (Extended Data Fig. 5c). Regions of necrosis, pseudopalisading necrosis and microvascular proliferation showed a lack of correlation with metabolically distinct areas (Extended Data Fig. 5d).

Fig. 2 | Identification of metabolic phenotypes in GB tumour sections.

a, Heatmap showing the average intensities of the seven metabolites used for segmentation of the three metabolic regions. **b**, Representative example of three tumour sections segmented into three clusters. The region containing state 3 cells (blue) showed high [U-¹³C]lactate and [U-¹³C]pyruvate labelling and was considered to have a glycolytic phenotype. The region containing state 2 cells (yellow) showed high labelling of [¹³C₂]glutamate and was considered to have an oxidative phenotype. The region containing state 1 cells (red) showed low labelling of glycolytic and TCA cycle metabolites. **c**, Metabolic segmentation based on spatial RNA sequencing of sections contiguous with those shown in **b**. Blue spots correspond to a glycolytic phenotype, and yellow spots correspond to an oxidative phenotype based on Hallmark gene sets. Red spots correspond to cells with low glycolytic and oxidative gene signatures. **d**, ATP/ADP and PCr/ATP signal intensity ratios (mean; error bars, s.d.) in normal-appearing brain ($n = 4$) and in the three metabolically defined regions (region 1, $n = 22$; region 2, $n = 14$; region 3, $n = 17$); every dot is a unique region. No statistical significance was identified using one-way ANOVA with Tukey's multiple comparisons test. **e**, Redox status (mean; error bars, s.d.) in normal-appearing brain tissue and GB regions quantified using AsA:DHA, GSH:GSSG and [U-¹³C]lactate/pyruvate

ratios (normal brain, $n = 4$; region 1, $n = 22$; region 2, $n = 14$; region 3, $n = 17$). No statistical significance was identified using one-way ANOVA with Tukey's multiple comparisons test. **f**, Quantification of Ki67⁺ cells, immune cells and blood vessels (mean; error bars, s.d.) in the three metabolically defined regions based on immunohistochemical analysis (region 1, $n = 17$; region 2, $n = 4$; region 3, $n = 8$). No statistical significance was identified using one-way ANOVA with Tukey's multiple comparisons test. **g**, Spatial co-assignment of deconvolved tumour/TME signals (first row) and MSI labels (second row). **h**, Violin plots showing tumour signal distribution by metabolic phenotype. Box plots display the median (50th percentile) as the central line, with boxes spanning the 25th and 75th percentiles. Whiskers extend to the minimum and maximum values within 1.5× the interquartile range; Glyco, $n = 5,440$; Low, $n = 8,038$; Oxphos, $n = 4,508$. **i**, Spatial uniform manifold approximation and projection (UMAP) plot of tumour-enriched spots from all metabolic phenotypes. **j**, Quantification of TME-deconvolved populations (x axis, population; y axis, normalized weight per spot for each phenotype). Box plot median and range as in **h**. **k**, Spatial maps showing that areas enriched for tumour cells display all three metabolic states. Highlighted areas show that these metabolic phenotypes arise from cells displaying strong tumour signals rather than from cells of the TME.



Tumour areas identified by a strong malignant signal in the spatial transcriptomics data showed the three metabolic states in spatially coherent areas on co-registered MS images (Fig. 2g–i), whereas regions identified as containing immune cells were predominantly glycolytic and those containing neurons were predominantly oxidative (Fig. 2j). Regions that showed a strong malignant signal and that were largely devoid of TME signals displayed all three metabolic states in the MS images (Fig. 2k). There were no differences in carbonic anhydrase IX (CAIX) transcript levels between the three metabolic states (Extended Data Fig. 6a), suggesting similar levels of hypoxia, or in immune, vascular, neuron, astrocyte and oligodendrocyte cell populations (Extended Data Fig. 6b).

The bioenergetic status and microenvironment of the three metabolic states indicate that differences in metabolic activity are unlikely to have been influenced by differences in tissue perfusion, the presence of necrosis, differences in cell proliferation or the presence of immune cell infiltrates, but rather represent tumour-cell-intrinsic metabolic phenotypes.

Phenotypes are not associated with vascularization

Despite there being no significant correlation between metabolic phenotype and blood vessel density, we nevertheless investigated a possible relationship between metabolic phenotype and proximity to the vasculature. We selected large vessels (Collagen I⁺ and α SMA⁺) (Extended Data Fig. 7a), co-registered these with contiguous MSI sections and measured ¹³C-labelled glycolytic and TCA cycle metabolites at 65 μ m intervals from the blood vessel lumen. Regardless of distance, there were no differences in lactate and glutamate labelling (Extended Data Fig. 7b), the number of proliferating cells, as indicated by Ki67⁺ staining (Extended Data Fig. 7c), the NADPH/NADP⁺ ratio (AsA:DHA ratio) or the NADH/NAD⁺ ratio ([U-¹³C]lactate/[U-¹³C]pyruvate ratio) (Extended Data Fig. 7d,e). However, there was a decrease in the number of immune cells with increasing distance from the vessel wall (Extended Data Fig. 7f,g).

Metabolic phenotypes are preserved in primary neurospheres

To confirm that the metabolic phenotypes are tumour-cell-intrinsic and not a consequence of differences in the TME, we derived 30 primary cell lines from 26 patients with GB (two patients had two cell lines derived from multi-regional tumour sampling). These were grown as neurospheres with [U-¹³C]glucose before snap-freezing and sectioning for MSI analysis (Fig. 3a–c). Three-dimensional culture has been shown to more closely approximate the behaviour of the primary tumour¹⁹. The MS images were segmented using the same *k*-means clustering as for the human data (Fig. 3d). The neurospheres derived from each cell line showed distinct metabolic states (Fig. 3a). Neurosphere diameter was similar for all three metabolic phenotypes, which showed similar AMP, ADP, ATP and PCr signal intensities and ATP/ADP ratios (Fig. 3e). Although the segmentation allowed us to group the spheres and the cells from which they were derived into distinct metabolic phenotypes, these nevertheless represent a continuum of glycolytic and TCA cycle activities (Extended Data Fig. 8a). RNA sequencing showed that spheres with a glycolytic phenotype had an upregulation of glycolytic genes and those regulated by hypoxia (Extended Data Fig. 8b). However, there was no difference in the oxidative or TCA cycle gene expression profiles.

Next, we looked at neurospheres derived from multi-regional sampling of the same tumour to determine whether the neurospheres captured the regional metabolic heterogeneity observed in the tumour samples. GTP2 Med (medial tumour) and GTP2 Lat (lateral tumour) formed similar-sized neurospheres but showed different metabolic phenotypes, with GTP2 Med being more glycolytic and clustering into state 3 and GTP2 Lat clustering into state 1. Similarly, AT21 Ant (anterior) and AT21 Post (posterior), from another patient, displayed an oxidative and mixed metabolic phenotype, respectively (Fig. 3f,g). Therefore, metabolic heterogeneity observed *in vivo* was retained following tissue dissociation and growth outside of the native TME.

To test the robustness of the tumour-cell-intrinsic metabolic phenotype, we grew a subset of neurospheres, representative of the highly glycolytic to the more oxidative phenotypes, under normoxic and hypoxic conditions (0.5% O₂) and compared their transcriptomes. Despite prolonged exposure to hypoxia (160 h), there was minimal change in the transcriptomes (Extended Data Fig. 8c). Gene set enrichment analysis of the PC1 loadings showed E2F and MYC targets and mTORC1 pathway genes in the top ten under both normoxic and hypoxic conditions, with hypoxia and glycolysis genes under normoxic conditions and oxidative phosphorylation, and epithelial mesenchymal transition genes under hypoxic conditions (Supplementary Table 4).

Neurosphere phenotypes were reproduced in rat brain

To further test the cell-intrinsic nature of the metabolic phenotypes, we implanted A11, AT8, S2 and AT5 into the brains of athymic rats and found that the cells retained the metabolic phenotypes that were observed when they were grown as neurospheres. AT8 and S2 formed more glycolytic xenografts, as demonstrated by higher [U-¹³C]lactate labelling, whereas AT5 xenografts were more oxidative with higher abundance of [¹³C₂]glutamate (Fig. 4a,b). There were no differences in cell proliferation (Ki67 staining), cell death (CC3 staining) or vascularization (CD3 staining) between these three models, which paralleled the finding in the human data that proliferation rate and vascularization were not responsible for the differences in the observed metabolic phenotypes (Extended Data Fig. 8d,e). We have shown previously that S2 cells are more sensitive than A11 cells to irradiation (referred to as GB1 and GB4, respectively, in the earlier publication²⁰) and that S2 xenografts are more sensitive than A11 xenografts to treatment with temozolomide plus irradiation²¹. Although when evaluated alongside all the other neurospheres, A11 and S2 appeared similarly glycolytic (Extended Data Fig. 8a), S2 xenografts showed greater TCA cycle activity than A11 xenografts (Fig. 4c,d). We have shown previously that A11 cells show higher glycolytic activity and S2 cells higher oxygen consumption and lower glycolytic activity, and demonstrated this in the corresponding xenografts using deuterium magnetic resonance spectroscopy and spectroscopic imaging measurements of deuterium-labelled glucose metabolism *in vivo*²². Treatment of cells with AZD2014 (mTOR1 and mTOR2 inhibitor)²³, imatinib (PDGFR; tyrosine kinase inhibitor)²⁴ and gefitinib (EGFR; tyrosine kinase inhibitor)²⁵ showed that cell viability was correlated with metabolic phenotype, where oxidative cells were more drug resistant (Extended Data Fig. 8f–h).

Phenotypes showed signatures in other pathways

The concentrations of unlabelled serine, threonine, glutamine and glutamate were significantly higher in oxidative regions in the patient tumour sections (ANOVA, Tukey's *P* < 0.05), and in the neurospheres, the concentrations of unlabelled leucine/isoleucine, glutamine, glutamate, histidine and phenylalanine were significantly higher (ANOVA, Tukey's *P* < 0.005) (Extended Data Fig. 9). The oxidative phenotype in GB has been associated with increased fatty acid oxidation⁵, and we observed that the concentrations of unlabelled fatty acids were higher in the more glycolytic regions in both the human and neurosphere data, as were intermediates in the pentose phosphate pathway.

Discussion

The extent to which tumour metabolism is driven by cell-intrinsic mechanisms or microenvironmental pressures is an open question in tumour biology⁶. To address this question, we measured the metabolic activity of GB within its native microenvironment using MS imaging of isotope labelling in rapidly quenched tissue from patients with GB. A similar approach has been used to map heterogeneity in fatty acid synthesis in gliomas implanted orthotopically in mice²⁶, to map metabolic activities in kidney and brain in mice²⁷ and to image glycolytic activity in a lung metastasis model²⁸.

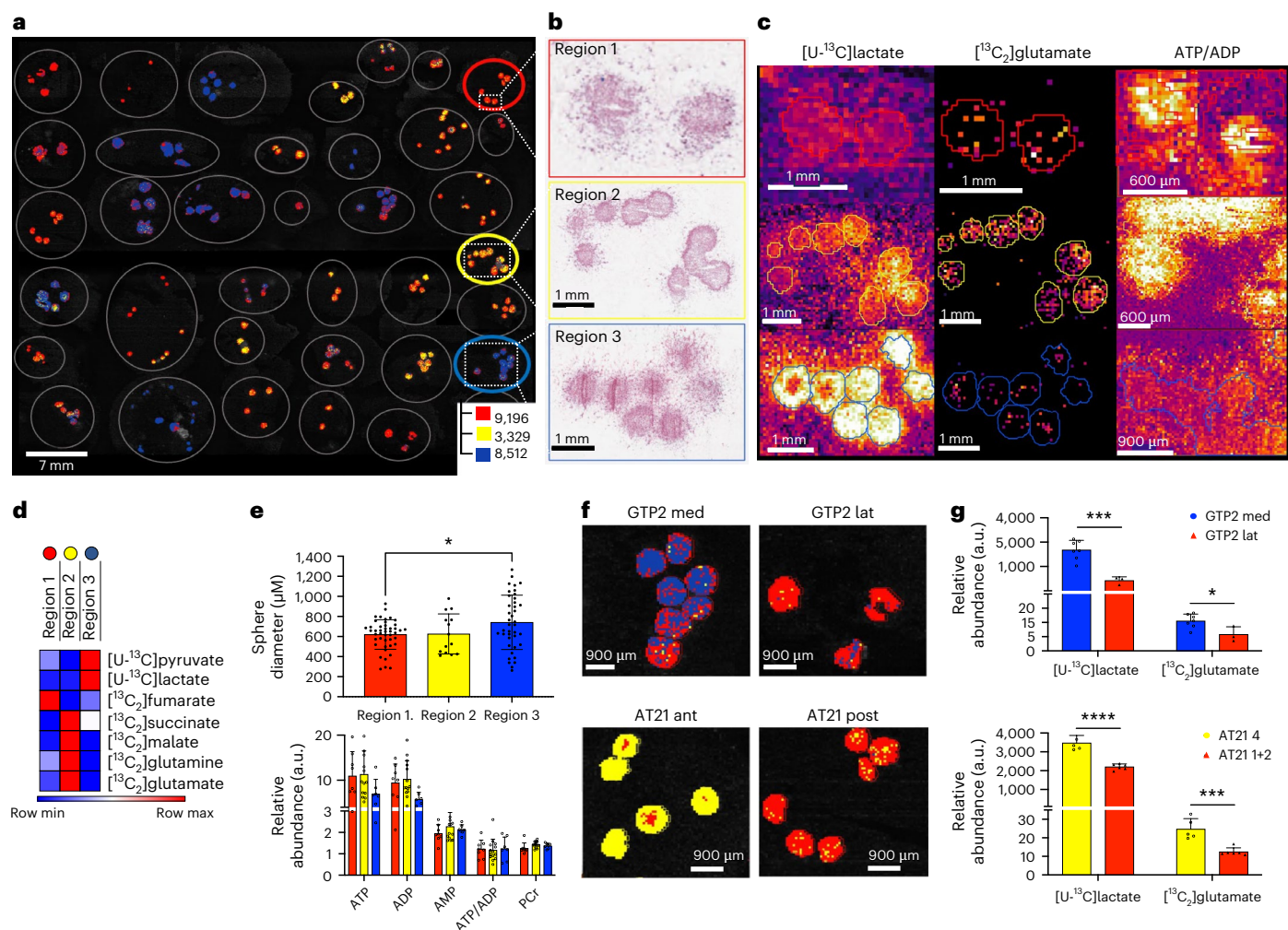


Fig. 3 | Primary neurospheres recapitulate metabolic phenotypes in patients with GB. **a**, *k*-means clustering map of 30 cell lines grown as neurospheres in Matrigel domes (outlined in grey) using the seven ^{13}C -labelled metabolites from glycolysis and the TCA cycle. Red corresponds to metabolic state 1 (low glycolytic, low TCA cycle activity), yellow corresponds to metabolic state 2 (high TCA cycle activity) and blue represents metabolic state 3 (high glycolytic activity). **b**, Representative H&E-stained sections of spheres displaying one of the three metabolic states. Red, yellow and blue outlines correspond to the sphere domes in **a**. **c**, Signal intensity maps for $[\text{U-}^{13}\text{C}]$ lactate, $[\text{C}_2\text{]}^{13}\text{C}$ glutamate and the ATP/ADP ratio in spheres shown in **b**. **d**, Heatmap showing the average signal intensities of the seven metabolites used for segmentation of the three metabolic states. **e**, Top: sphere diameter for each metabolic phenotype. Each

point represents a single sphere. State 3 (glycolytic phenotype) had a higher average sphere diameter than state 1 (low glycolytic, low TCA cycle activity) ($P = 0.027$). Bottom: ATP, ADP, AMP and PCr signal intensities in neurospheres with different metabolic phenotypes. **f**, *k*-means segmentation of MS images of spheres derived from multi-regional tumour sampling (GTP2 and AT21). These results are part of the *k*-means analysis performed on all 30 neurosphere lines. **g**, Signal intensities of $[\text{U-}^{13}\text{C}]$ lactate and $[\text{C}_2\text{]}^{13}\text{C}$ glutamate in the indicated neurospheres ($****P < 0.0001$). The colour of the bar corresponds to the metabolic phenotype. Data are means; error bars, s.d.; each dot represents a single neurosphere. Asterisks refer to *P* values obtained from one-way ANOVA followed by Tukey's multiple comparisons test or unpaired *t*-test ($*P < 0.05$, $***P < 0.0005$, $****P < 0.00005$).

Using a targeted approach, we identified distinct glycolytic and oxidative metabolic phenotypes. Although recent reports have identified metabolic phenotypes from a transcriptomic analysis⁵, we describe here the classification of metabolic phenotypes based on measurements of metabolic activity in patient tumours in vivo at relatively high spatial resolution (65 μm). The metabolic phenotypes occupied distinct territories that did not show significant differences in the cellular composition of their microenvironments, including immune cell infiltration, proliferative index and vascularization. The presence of these metabolic phenotypes in distinct territories and their cellular composition was confirmed by spatial transcriptomics. Importantly, we have shown that these tumour-cell-intrinsic metabolic phenotypes can be independent of the TME. Previous studies have also shown that tumour subtype-specific protein²⁹ and gene expression profiles³⁰ can be independent of the tumour niche.

We observed no change in lactate and glutamate labelling with distance from the blood vessels. This appears to be inconsistent with a study in an orthotopically implanted glioma cell line model (U87MG) in immunocompromised mice that showed high mitochondrial activity in cells adjacent to vessels and increased expression of hypoxia-related genes at increasing distance from the vessels. However, there were no significant increases in lactate concentration or differences in α -ketoglutarate concentrations in the cells with distance from the vessels in this study, although these concentrations may have been affected by the flow cytometric method used to sort the cells³¹. An MSI study on an orthotopically implanted syngeneic murine model of isocitrate dehydrogenase 1 mutant GB in animals fed for 48 h with $[\text{U-}^{13}\text{C}]$ glucose showed a remarkable degree of metabolic homogeneity in the tumours³², in contrast to what was observed here in tumours from patients with GB, emphasising the significance of the observed metabolic phenotypes.

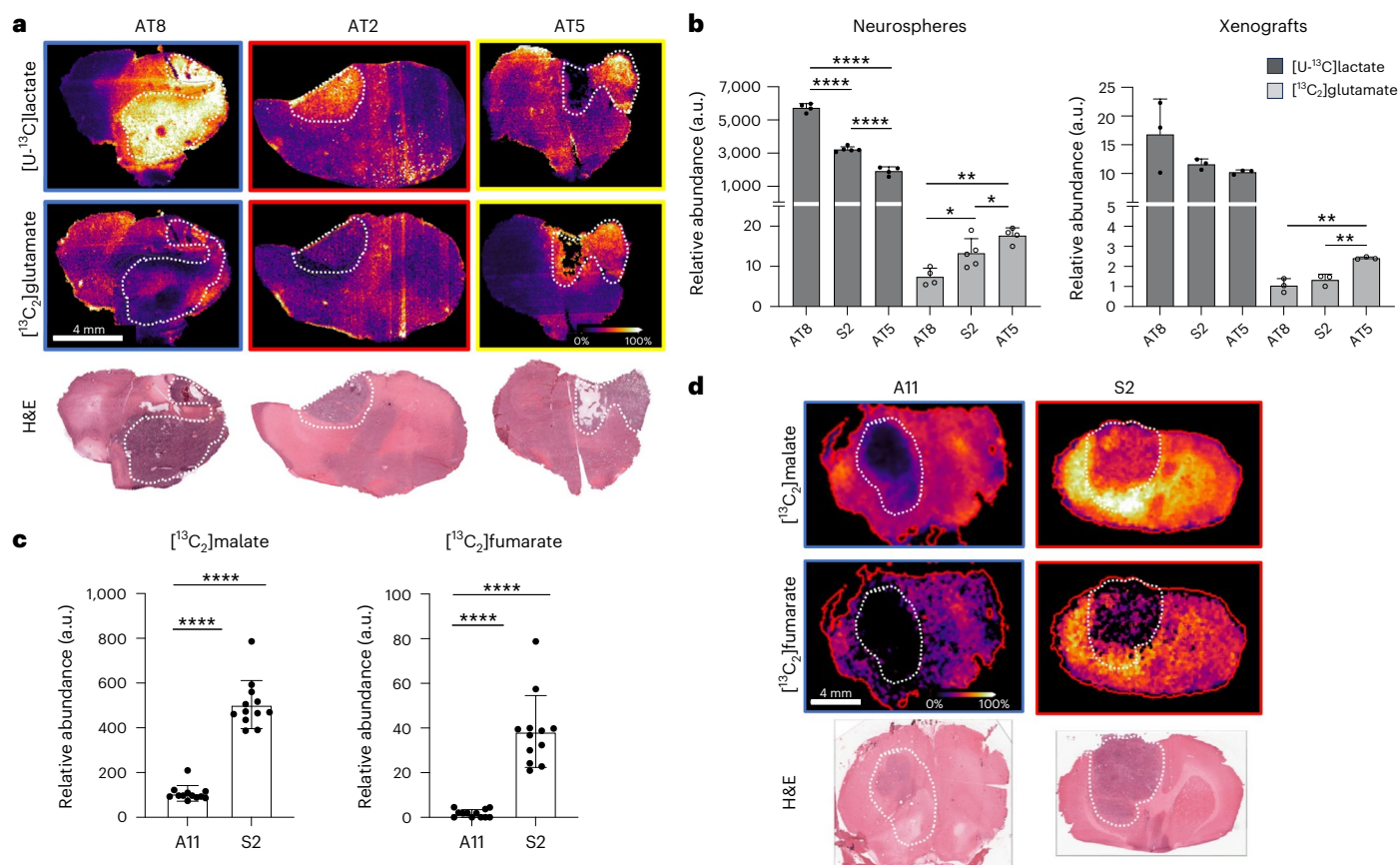


Fig. 4 | Neurospheres retain their metabolic signatures as orthotopically implanted xenografts, and these signatures correlate with drug response.

a, Representative MSI sections from rat brains implanted with AT8, S2 and AT5 ($n = 3$ independent tumours per model). Relative signal intensities for [U-¹³C] lactate (top) and [¹³C₂]glutamate (bottom); H&E-staining of the corresponding sections. **b**, The relative signal intensities of [U-¹³C]lactate (**** $P < 0.0001$) and [¹³C₂]glutamate (AT8 vs AT5, $P = 0.0012$; S2 vs AT5, $P = 0.0406$; AT8 vs AT5, $P = 0.0012$) in neurospheres (AT8, $n = 4$; S2, $n = 5$; AT5, $n = 4$) and the respective

xenografts (AT8, $n = 3$; S2, $n = 3$; AT5, $n = 3$) expressed as mean values; error bars, s.d. ([¹³C₂]glutamate AT8 vs AT5, $P = 0.0015$; S2 vs AT5, $P = 0.0049$). * $P < 0.05$; ** $P < 0.005$. **c**, Relative abundance (mean values; error bars, s.d.) of labelled malate and fumarate in sections of A11 and S2 xenografts. **d**, Top: labelled malate and fumarate signal intensities in MS images of the brains of rats implanted with A11 ($n = 12$) and S2 ($n = 12$) xenografts. Bottom: H&E-staining of the corresponding sections. Asterisks refer to P values obtained from one-way ANOVA followed by Tukey's multiple comparisons test or unpaired t -test (**** $P < 0.0001$).

The cell-intrinsic nature of the metabolic phenotypes was confirmed using neurospheres grown in vitro, which reproduced the metabolic phenotypes observed in the patients and were preserved following their orthotopic implantation in rats. Exposing the neurospheres to chronic hypoxia did not lead to significant changes in the neurosphere transcriptomes, demonstrating the robustness of these phenotypes and further underlining their independence from the TME. This is in contrast to a similar study in patients with lung cancer who were infused with [U-¹³C]glucose, which concluded that given the observed differences in glucose oxidation in the TCA cycle in well-perfused versus poorly perfused regions, tumour perfusion in this case overrides tumour-cell-intrinsic metabolic phenotypes³³.

A recent study in mouse models of leukaemia, pancreatic, lung and colon cancer showed that these tumours suppress TCA cycle activity relative to normal tissue. By contrast, the glutamate labelling observed here in the GB tumours was similar to that in normal-appearing brain. Similar observations of substantial glucose oxidation in the TCA cycle have been made previously in human lung tumours³³ and in non-imaging studies of patients with GB who were infused with [U-¹³C]glucose⁷.

Metabolic phenotypes with distinct therapeutic vulnerabilities have been identified in several cancers^{34–38}, including GB⁵, in which GB cells with an oxidative phenotype were shown to be more sensitive to inhibitors of mitochondrial complex I and to radiation treatment. We have shown previously that S2 cells are more sensitive to irradiation in vitro²⁰ and in vivo²¹ and have shown here, and previously, that

they have a more oxidative phenotype with higher TCA cycle activity than A11 cells, which show a more glycolytic phenotype. Previous RNA sequencing studies have shown that A11 has a mesenchymal phenotype, whereas S2 cells have a neural progenitor cell-like phenotype³⁹, consistent with a previously identified association between the mesenchymal and glycolytic phenotypes⁵.

Cells displaying these distinct metabolic phenotypes occupy territories that are sufficiently large to be imaged clinically using techniques such as hyperpolarized ¹³C magnetic resonance imaging (MRI)⁴⁰ and deuterium metabolic imaging⁴¹. These metabolic phenotypes show a correlation with treatment responsiveness, suggesting that a personalized therapy approach may be possible in which metabolic imaging and phenotyping could be used to guide subsequent treatment selection.

We have demonstrated here high-resolution imaging of isotope labelling of cellular metabolites in a human tumour in vivo. In conjunction with studies on patient-derived neurospheres and orthotopically implanted xenografts, we have demonstrated the presence of different metabolic phenotypes within GB that are tumour-cell-intrinsic and largely independent of the TME.

Methods

Patient samples and ethical approval

Three male patients from Addenbrooke's Hospital, Cambridge, were infused with [U-¹³C]glucose. The selection criteria included first clinical presentation, MRI consistent with GB and no significant co-morbidities.

Following induction of anaesthesia, a pyrogen-free 5% solution of [^{13}C]glucose in sterile saline (Merck) was administered as a bolus of 8 g over 10 min followed by 8 g h⁻¹ continuous infusion, as described previously for patients with GB⁷ and several other tumour types⁴². Arterial blood was collected by a peripheral arterial line before bolus administration and then every 15 min following the start of infusion and at 15 min after the end of the infusion. Tumour sampling was guided by intra-operative Stealth navigation^{43–45} and assessment of 5-ALA fluorescence. Tumours were sampled between 90 and 150 min⁷. A pituitary rongeur was used to transfer tumour samples directly into liquid nitrogen. The freezing time was <5 s between tissue devascularization and immersion in liquid nitrogen.

The study was approved by the Central Cambridge Research Ethics Committee and was compliant with the Health Research Authority. The study adhered to the principles of the Declaration of Helsinki and the Guidelines for Good Clinical Practice. Participants did not receive financial compensation and gave informed consent.

Tissue preparation

Frozen tumour samples were embedded in a hydroxypropyl methylcellulose/polyvinylpyrrolidone hydrogel⁴⁶, and 10 μm -thick cryo-sections were obtained. Sections were thaw-mounted onto Superfrost microscope slides for desorption electrospray ionization (DESI) and IMC experiments (Thermo Scientific), while sections prepared for MALDI-MSI were thaw-mounted onto conductive ITO-coated slides (Bruker Daltonik). The sections were dried immediately and sealed in vacuum pouches for storage at $-80\text{ }^\circ\text{C}$. Human tumour samples were treated with UV-C light before MSI analysis to minimize aerosolization of potential pathogens. Decontamination was performed in a sensor-controlled UV chamber (Opsytec Dr. Gröbel) at 250 mJ cm⁻².

MSI

DESI-MSI analysis was performed on a Q-Exactive mass spectrometer (Thermo Scientific) equipped with an automated 2D-DESI ion source (Prosolia). The spectrometer was used with a home-made Swagelok DESI sprayer and a mixture of 95% methanol, 5% water delivered at a flow rate of 1.5 $\mu\text{l min}^{-1}$ and nebulized with nitrogen at a backpressure of 6 bar. Human tumour samples were analysed in the mass range from 70 to 280 m/z with a mass resolution of 140,000 at 200 m/z . The injection time was set at 500 ms, and data were acquired with a pixel size of 65 μm . Following analysis, sections were stained with H&E and co-registered with the DESI-MS images. The resulting .raw files were converted into .mzML files using ProteoWizard msConvert (v.3.0.4043) with the built-in peak picking algorithm⁴⁷ and subsequently compiled to an .imzML file (imzML converter, v.1.3)⁴⁸. All subsequent data processing was performed in SCiLS Lab (v.2022b, Bruker Daltonik).

MALDI-MSI analysis was performed using a Rapiflex Tissue typer instrument (Bruker Daltonik) operated in negative ion detection mode. 9-Aminoacridine, prepared in an 80:20 methanol-to-water ratio, was used as a matrix and spray-deposited using an automated spray system (M3-Sprayer, HTX technologies). Mass spectra were acquired from 180 to 1,000 m/z with a pixel size of 40 μm . A total of 350 laser shots were summed up per pixel. For all experiments, the laser was operated with a repetition rate of 10 kHz. Raw data were directly uploaded and processed with SCiLS Lab (v.2022b) software.

DESI and MALDI data and images were normalized to the total ion current to compensate for signal variation during the course of the experiments, and acquisition parameters and data processing were identical for human tissue, neurospheres embedded in Matrigel and xenograft sections.

³¹P NMR spectroscopy of tumour extracts

Snap-frozen tumour samples were homogenized with 5 $\mu\text{l mg}^{-1}$ of 2 M perchloric acid. The extract was centrifuged at 13,000g for 15 min, and the pH of the supernatant was adjusted to 7.0 using 2 M KOH. Extracts

were lyophilized and dissolved in 550 μl deuterium oxide containing methylenediphosphonic acid at 100 nmol g⁻¹ tissue, which was added as a chemical shift and intensity standard. Proton-decoupled ³¹P NMR spectra were acquired with more than 8,000 repetitions into 32,768 data points with an 11 μs 90° pulse, a repetition time of 7.2 s and a spectral width of 57 ppm (14,006 Hz).

Liquid chromatography–MS plasma analysis

Arterial blood collected during intra-operative infusion was centrifuged at 2,000g and 4 $^\circ\text{C}$ for 20 min to collect the plasma, which was snap-frozen and stored at $-80\text{ }^\circ\text{C}$. Samples were thawed on wet ice and aliquots diluted 50-fold with cold methanol:acetonitrile:water (50:30:20) in chilled tubes, vortexed for 10 min and centrifuged at 21,100g for 10 min at 4 $^\circ\text{C}$, and then the supernatants stored at $-80\text{ }^\circ\text{C}$. On the day of analysis, supernatants were centrifuged and aliquots transferred to a 96-well plate for analysis by hydrophilic interaction liquid chromatography (HILIC) high-resolution mass spectrometry (HRMS).

The HILIC–HRMS system consisted of a Shimadzu Nexera X2 UHPLC and Sciex 6600 Triple TOF mass spectrometer, using a SeQuant ZIC-pHILIC 5 μm 150 \times 2.1 mm column (with a ZIC-pHILIC 20 \times 2.1 mm guard column) at 45 $^\circ\text{C}$. The liquid chromatography gradient started at 80% acetonitrile and 20% 20 mM ammonium carbonate (pH 9.4), changing to 20% acetonitrile over 17 min at 200 $\mu\text{l min}^{-1}$, with a further 11.5 min of column re-equilibration. Each sample was injected twice for analysis in both positive and negative electrospray ionization with a full-scan m/z range of 75–1,000.

Data were acquired using Sciex Analyst TF and processed using Sciex MultiQuant software. Extracted ion chromatograms were generated from the theoretical $m/z \pm 20$ ppm. Peak integration was reviewed manually, and the peak area of each metabolite and isotope was exported.

Neurosphere cell line derivation and MSI preparation

Primary human cell lines were derived at Addenbrooke's Hospital, Cambridge, UK, as described previously⁴⁹. Tissue collection was approved by a Regional Ethics Committee (REC18/EE/0283) and was compliant with the UK Human Tissue Act 2004. Resected tissue samples were washed with Hanks' balanced salt solution and minced using sterile razor blades, followed by digestion with Accutase (Sigma-Aldrich) for 60 min at 37 $^\circ\text{C}$. Single cells were isolated by filtration through a 40 μm filter (Falcon). Cells were centrifuged at 350g, 21 $^\circ\text{C}$, and the pellet was incubated with 2–3 ml of Red Blood Cell Lysis Buffer (Sigma-Aldrich) for 5 min at room temperature (21 $^\circ\text{C}$). Following centrifugation, cells were seeded at a density of 15,000 cells per cm² in serum-free Neurobasal A medium (Gibco) supplemented with B27, N2, EGF and FGF growth factors (Sigma-Aldrich). Cells were allowed to form aggregates, and the medium was changed 3 days post derivation⁵⁰.

For neurosphere formation, cells were seeded in Ultra Low Attachment 96-well plates (Corning) at a density of 10,000 cells per well. Sphere diameter was monitored using an IncuCyte microscope (Sartorius). Spheres were embedded in 150 μl Matrigel (Corning) domes in 24-well plates (Corning). The domes were covered with 2 ml of fresh Neurobasal medium and grown for 24 h. The domes were then washed three times with PBS before 2 ml of fresh glucose-free Neurobasal medium supplemented with 25 mM [^{13}C]glucose was added. Following incubation for 24 h, the medium was removed and the domes were washed three times with ice-cold PBS and then snap-frozen in liquid nitrogen. The domes were sectioned to a thickness of 10 μm and analysed using DESI-MSI and MALDI-MSI, as described above.

Drug treatment of primary cells

Black, clear-bottomed 96-well plates (Corning) pre-coated with ECM (Merck) were seeded at 5,000 cells per well and incubated at 37 $^\circ\text{C}$ in 200 μl of Neurobasal medium supplemented with growth factors, as described above. The medium was then replaced with either fresh

medium or medium containing the following drug concentrations: AZD2014, 1 μM ; gefitinib, 1 μM ; imatinib, 10 μM . The cells were incubated for 72 h before re-imaging using the IncuCyte microscope, and cell numbers were determined using the Sartorius cell confluency module. At the end of the incubation, the medium was aspirated, and 100 μl of PBS containing 3 μM propidium iodide was added to each well to measure necrotic cell death. The plates were imaged using the IncuCyte 10 \times cell-by-cell module using the red channel. The experiment was repeated three times with six technical replicates for each drug treatment.

RNA sequencing of neurospheres

Neurospheres in Matrigel domes were grown at 37 °C, with one plate incubated in atmospheric O₂ and the other grown in 0.5% O₂, 0.5 Pa (Avatar, XCellbio). Medium was refreshed every 48 h, and on day 10 it was removed, the plates placed on ice and the wells washed with 1 ml of ice-cold PBS, followed by the addition of 1 ml Corning Cell Recovery Solution. The plates were incubated at 4 °C for 1 h and then washed four times with ice-cold PBS. RNA was isolated from cell pellets using a QIAshredder spin column (Qiagen) and AllPrep DNA/RNA Mini Kit (Qiagen), quantified using a Qubit fluorometer (Thermo Fisher Scientific) and quality tested using an Agilent 4200 TapeStation. For library preparation, the Illumina TruSeq Stranded mRNA Kit was used, and single-read sequencing was performed on a HiSeq 4000 machine (Illumina). Quality control of raw sequence data was carried out using FastQC (v.0.11.8). Some reads were trimmed to remove adaptor content using Trimmomatic (v.0.39)⁵¹. Reads were aligned to GRCh38 Ensembl release 102 using STAR (v.2.7.7a)⁵² and alignment quality control was carried out using Picard tools (v.2.25.1). Quantification was carried out using Salmon (v.1.6.0) against a reference transcriptome for the same genome release. Differential gene expression analysis was carried out in R (v.4.2.2) using the DESeq2 package (v.1.38.3)⁵³ with default parameters. Multiple testing correction of *P* values was carried out using the Benjamini–Hochberg method⁵⁴. Genes were determined to be differentially expressed at an adjusted *P* value of 0.05. Gene set enrichment analysis was carried out using clusterProfiler (v.4.6.0)⁵⁵.

Patient-derived xenografts and [U-¹³C]glucose infusion

Experiments were performed under the authority of a Home Office project licence (PP5634271) and approved by an Animal Welfare and Ethical Review Body at the Cancer Research UK (CRUK) Cambridge Institute, University of Cambridge. Athymic, female nude rats that were at least 9 weeks old were implanted orthotopically with the primary GB lines at passage 10. Animals were anaesthetized using 2% isoflurane (Isoflo, Abbott Laboratories) in O₂/air (25/75%, vol/vol, 2 l min⁻¹) with 5 mg kg⁻¹ Carprofen (Zoetis) and 0.3 mg ml⁻¹ buprenorphine hydrochloride (Alstoe) subcutaneous analgesia. Body temperature was maintained using a heating pad. A stereotactic surgical frame (Kopf) was used to secure the animal's head. A midline incision was made followed by a 1 mm burr hole anterior and to the right of the bregma. A total of 1 \times 10⁶ cells were injected in 5 μl of Neurobasal medium at a depth of 4 mm. The burr hole was closed with bone wax (Ethicon) and skin with 6/0 vicryl (Ethicon). Tumour growth was monitored using T₂-weighted MRI. Specifically, animals were anaesthetized using 2% isoflurane (Isoflo, Abbott Laboratories) in O₂/air (25/75%, vol/vol, 2 l min⁻¹) and placed supine inside a 7T magnet (Agilent), and T₂-weighted MRI was used to monitor tumour growth. A 72 mm ¹H volume coil was placed around the animal's head, and breathing rate and temperature were monitored with a small animal instruments monitoring system (SAII). Axial ¹H T₂-weighted images were acquired using a fast spin-echo sequence with an echo time of 50 ms, pulse repetition time of 1,500 ms, flip angle of 60–90° and a slice thickness of 2.0 mm, field-of-view of 40 mm \times 40 mm and 128 \times 128 or 256 \times 256 data points.

Three animals per cell line were administered with [U-¹³C]glucose as a bolus at 0.4 mg g⁻¹, followed by continuous infusion of

0.012 mg g⁻¹ min⁻¹ at 300 μl h⁻¹ for 120 min (ref. 56). The brains were snap-frozen in liquid nitrogen, cryo-sectioned at a thickness of 10 μm and analysed with DESI-MSI and MALDI-MSI, as described above.

Spatial transcriptomic data acquisition and analysis

The 10 \times Genomics Visium platform was used and analysed with the Space Ranger pipeline. Downstream analyses were conducted in R using the Seurat package⁵⁷. Samples were processed individually using the SCTransform() function. Spots were filtered based on standard quality control thresholds (for example, mitochondrial gene percentage of >20%, nCount_Spatial of <1,000 and nFeature_Spatial of <1,000). Data were re-corrected across samples using PrepSCTFindMarkers() for joint numerical analyses. Gene set scoring was performed using the Hallmark gene sets and the UCELL package⁵⁸, excluding mitochondrial genes from the oxidative phosphorylation score calculations. To annotate spatial spots, genes from Hallmark gene sets of interest were combined and subjected to *k*-means clustering (*k* = 3).

To annotate TME spots, we performed two deconvolution steps with robust cell type decomposition⁵⁹, using previously published reference cell annotations⁶⁰. First, a balanced normal reference was sampled from the non-neoplastic cells, combined with the neoplastic cells and used as input for robust cell type decomposition. The assignment was further confirmed by histological evaluation. To label TME niches, we further deconvolved TME signals into oligodendrocytes, astrocytes, vascular cells, immune cells (macrophages) and neurons. Given that each spatial spot contained multiple cells, we normalized the deconvolution weights to a maximum of one, providing a relative abundance. To mitigate over-assignment to sorted TME cell types, we included unsorted cell types (neoplastic + oligodendrocyte precursor cell with high transcriptomic similarity) in this deconvolution step as a 'block' effect. Joint feature plots (tumour and TME) were generated using a custom modification of the SpatialFeaturePlotBlend() source function. The original repository is available at <https://github.com/george-hall-ucl/SpatialFeaturePlotBlend>. For the TME population-level quantification, for each spot, the weights of all deconvolved populations were normalized to sum to one, thereby representing the relative contribution of each cell population within that specific spot. Subsequently, these normalized weights were plotted across the three metabolic states.

MSI and spatial transcriptomic data co-registration

Total ion count-normalized MSI data were extracted using the SCiLS Lab API (v.2022b; Bruker Daltonik), and metabolic labels were spatially smoothed to provide coherent spatial regions. Immediately neighbouring pixels (≤ 8) were identified for each MSI pixel, and across five iterations, for each pixel that had at least two neighbours and for which the majority of neighbours were assigned a different label, the label was replaced with the majority label. An image was created using spatial coordinates, in which pixels were coloured using the first three principal components as RGB channels. Landmarks were identified between this MSI dimensionality reduction image and the H&E image of the corresponding tissue section, and subsequently between the H&E image and the corresponding H&E image of the contiguous tissue section used for spatial transcriptomic analysis. These landmarks were then used to map the MSI coordinates onto the spatial transcriptomic coordinate space using an affine transform. MSI labels were finally transferred to spots on the spatial transcriptomic image using the *k*-nearest neighbours algorithm (*k* = 3).

Defining metabolic regions on MSI

Regions were defined using *k*-means clustering and fitted using the *Kmeans* function in the *amap* R package and performed independently on the neurosphere, human and metastases datasets. The values for each of the seven ¹³C-labelled metabolites used for metabolic clustering were standardised into *z*-scores (by subtracting the metabolite's mean

and dividing by the metabolite's standard deviation). Each pixel was then assigned to three or four groups, using *k*-means clustering with Manhattan distances.

IMC and immunohistochemistry

Antibodies used for immunohistochemistry are described in Supplementary Table 5. Antibodies were tagged using the Fluidigm Maxpar Antibody Labelling Kit. Slides were fixed with 4% paraformaldehyde in PBS for 10 min, washed three times in PBS, permeabilized using a 1:1,000 dilution of Triton X-100 in casein solution, washed another three times in PBS and then blocked for 30 min with casein solution (Thermo Fisher). Antibodies were diluted in casein solution, and the slides were incubated overnight at 4 °C. The slide was then washed three times in PBS, and nuclei were stained with DNA intercalator-iridium (Fluidigm) at a dilution of 1:400 in PBS for 30 min. The slide was washed three times in PBS, 30 s in deionized water and then dried at room temperature. A region for IMC analysis was selected using consecutive H&E-stained sections and the DESI-MSI data. IMC analysis was performed using a Hyperion Instrument (Fluidigm Corporation) with an ablation energy of 4 db and an ablation frequency of 200 Hz. IMC images were produced using MCD viewer (v.1.0; Fluidigm), and analysis was performed using HALO (Indica Labs).

Tumour-bearing rat brains were snap-frozen in liquid nitrogen and sectioned at 6 µm thickness for immunohistochemistry analysis using Leica's Polymer Refine Kit (antibodies listed in Supplementary Table 6). Images were analysed using Aperio image-viewing software and HALO (v.3.6.4134.137).

HALO image analysis

HALO (v.3.6.4134.137) and HighPlex FL (v.4.1.3) modules were used for automated image analysis. Optical densities for weakly, moderately and strongly stained cells used for the automated quantitative analysis of scanned sections were as follows: Ki67 – (nuclear) 7, 40.7522, 54.385, p53 – (nuclear) 1.8, 3.5929, 5.1327, CC3 – (cytoplasm) 1.9427, 4.646, 6.1947, Vimentin – (cytoplasm) 13.3343, 25.7522, 41.2035, CD3 – (nuclear) 2.2832, 32.6875, 63, GZMB – (nuclear) 0.6956, 0.8673, 1.6106, CD4 – (cytoplasm) 3.9823, 6.7699, 10.354, CD8A – (nuclear) 1.6327, 18.7679, 26, CD68 – (cytoplasm) 10.4106, 45.9027, 78.6903, CD45 – (cytoplasm) 2, 5.3363, 7.115, ASMA – (cytoplasm) 2.8, 12.1327, 18.6239, CD31 – (cytoplasm) 2.274, 4.5841, 6.876, panCK – (cytoplasm) 1.836, 2.8673, 3.9823, Collagen I – (cytoplasm) 28.293, 104.7301, 179.58.

Five cellular phenotypes were identified: CD4⁺ helper T cells (CD45⁺CD4⁺CD3⁺); cytotoxic T cells (CD3⁺CD45⁺CD8A⁺); activated cytotoxic T cells (CD3⁺CD45⁺CD8A⁺GZMB⁺); natural killer cells and neutrophils (CD45⁺GZMB⁺); and macrophages and microglia (CD68⁺). A random forest classifier was used to distinguish vessels and non-vessels within the images. Large vessels were positive for Collagen I and CD31. Annotations were created manually on several images, and these were used to train the classifier. The five cellular phenotypes were plotted spatially, three 60 µm bands travelling out from the vessels were defined and the total number of cells displaying these cellular phenotypes in each band was determined.

Statistical analyses

Sample size for human tumour collection was determined intra-operatively based on patient and tumour factors (for example, proximity to eloquent brain). A minimum of six samples were collected for each tumour region. For xenograft and neurosphere studies, a minimum of three independent biological replicates were used (three different rats; three different cell line passages with a minimum of six technical replicates). No randomization or blinding was used, and all data were included in the analysis. Statistical analyses were performed using GraphPad Prism (v.10.0.3), R (v.4.3.0) and SciLS. Bioinformatics analyses were performed in R. Statistical tests were two-sided unless stated otherwise. Student's *t*-tests and one-way ANOVA with Tukey's

multiplicity correction were used to test the equality of means between two or more groups, respectively.

Reporting summary

Further information on research design is available in the Nature Portfolio Reporting Summary linked to this article.

Data availability

The raw and processed RNA sequencing and MSI data that are not derived from GB patient material are available at the following links: RNA sequencing data are available at <https://www.ncbi.nlm.nih.gov/geo/GSE288836>; the spatial transcriptomics RNA object (seura_obj.RDATA) is available at <https://doi.org/10.17863/CAM.116214>; and the MSI data are available at <https://www.ebi.ac.uk/metabolights/MTBLS12176>. The authors defer deposition of raw MSI data derived from GB patient material to ensure compliance with legal requirements of the University of Cambridge and Cambridge University Hospitals NHS Foundation Trust and avoid compromising the privacy of the study participants. Requests for raw data can be referred to the corresponding authors; these will be reviewed within ten working days in consultation with the institutional R&D, which will determine the terms of a data transfer agreement between the recipient institution, the University of Cambridge and Cambridge University Hospitals NHS Foundation Trust. Source data are provided with this paper.

References

1. Verhaak, R. G. et al. Integrated genomic analysis identifies clinically relevant subtypes of glioblastoma characterized by abnormalities in PDGFRA, IDH1, EGFR, and NF1. *Cancer Cell* **17**, 98–110 (2010).
2. Wang, Q. et al. Tumor Evolution of Glioma-Intrinsic Gene Expression Subtypes Associates with Immunological Changes in the Microenvironment. *Cancer Cell* **32**, 42–56.e6 (2017).
3. Neftel, C. et al. An integrative model of cellular states, plasticity, and genetics for glioblastoma. *Cell* **178**, 835–849.e21 (2019).
4. Wen, P. Y. & Kesari, S. Malignant gliomas in adults. *N. Engl. J. Med.* **359**, 492–507 (2008).
5. Garofano, L. et al. Pathway-based classification of glioblastoma uncovers a mitochondrial subtype with therapeutic vulnerabilities. *Nat. Cancer* **2**, 141–156 (2021).
6. Kim, J. & DeBerardinis, R. J. Mechanisms and implications of metabolic heterogeneity in cancer. *Cell Metab.* **30**, 434–446 (2019).
7. Maher, E. A. et al. Metabolism of [¹³C]glucose in human brain tumors in vivo. *NMR Biomed.* **25**, 1234–1244 (2012).
8. Williams, G. D., Palmer, C., Heitjan, D. F. & Smith, M. B. Allopurinol preserves cerebral energy metabolism during perinatal hypoxia-ischemia: a ³¹P NMR study in unanesthetized immature rats. *Neurosci. Lett.* **144**, 103–106 (1992).
9. Veech, R. L., Lawson, J. W., Cornell, N. W. & Krebs, H. A. Cytosolic phosphorylation potential. *J. Biol. Chem.* **254**, 6538–6547 (1979).
10. Timm, K. N. et al. Assessing oxidative stress in tumors by measuring the rate of hyperpolarized [¹³C]dehydroascorbic acid reduction using ¹³C magnetic resonance spectroscopy. *J. Biol. Chem.* **292**, 1737–1748 (2017).
11. Williamson, D. H., Lund, P. & Krebs, H. A. The redox state of free nicotinamide-adenine dinucleotide in the cytoplasm and mitochondria of rat liver. *Biochem. J.* **103**, 514–527 (1967).
12. Aniansson Zdolsek, H., Ernerudh, J., Holt, P. G., Nilsson, J. & Björkstén, B. Expression of the T-cell markers CD3, CD4 and CD8 in healthy and atopic children during the first 18 months of life. *Int. Arch. Allergy Immunol.* **119**, 6–12 (1999).
13. Ledbetter, J. A. et al. CD4, CD8 and the role of CD45 in T-cell activation. *Curr. Opin. Immunol.* **5**, 334–340 (1993).

14. Wever, P. C. et al. The CD8⁺ granzyme B⁺ T-cell subset in peripheral blood from healthy individuals contains activated and apoptosis-prone cells. *Immunology* **93**, 383–389 (1998).
15. Krzywinska, E. et al. CD45 isoform profile identifies natural killer (NK) subsets with differential activity. *PLoS ONE* **11**, e0150434 (2016).
16. Nuovo, J. in *In Situ Molecular Pathology and Co-Expression Analyses* (ed G. J. Nuovo) 167–196 (Academic, 2013).
17. Mustafa, D. et al. Expression sites of colligin 2 in glioma blood vessels. *Brain Pathol.* **20**, 50–65 (2010).
18. Schmidt, D. & von Hochstetter, A. R. The use of CD31 and collagen IV as vascular markers. A study of 56 vascular lesions. *Pathol. Res. Pract.* **191**, 410–414 (1995).
19. Riedel, N. C., de Faria, F. W., Alfert, A., Bruder, J. M. & Kerl, K. Three-dimensional cell culture systems in pediatric and adult brain tumor precision medicine. *Cancers* **14**, 5972 (2022).
20. Mair, R. et al. Metabolic imaging detects low levels of glycolytic activity that vary with levels of c-Myc expression in patient-derived xenograft models of glioblastoma. *Cancer Res.* **78**, 5408–5418 (2018).
21. Hesse, F. et al. Imaging glioblastoma response to radiotherapy using ²H magnetic resonance spectroscopy measurements of fumarate metabolism. *Cancer Res.* **82**, 3622–3633 (2022).
22. Low, J. C. M. et al. Deuterium metabolic imaging differentiates glioblastoma metabolic subtypes and detects early response to chemoradiotherapy. *Cancer Res.* **84**, 1996–2008 (2024).
23. Guichard, S. M. et al. AZD2014, an inhibitor of mTORC1 and mTORC2, is highly effective in ER+ breast cancer when administered using intermittent or continuous schedules. *Mol. Cancer Ther.* **14**, 2508–2518 (2015).
24. Dong, Y. et al. Selective inhibition of PDGFR by imatinib elicits the sustained activation of ERK and downstream receptor signaling in malignant glioma cells. *Int. J. Oncol.* **38**, 555–569 (2011).
25. Vansteenkiste, J. Gefitinib (Iressa): a novel treatment for non-small cell lung cancer. *Expert Rev. Anticancer Ther.* **4**, 5–17 (2004).
26. Buglakova, E. et al. Spatial single-cell isotope tracing reveals heterogeneity of de novo fatty acid synthesis in cancer. *Nat. Metab.* **6**, 1695–1711 (2024).
27. Wang, L. et al. Spatially resolved isotope tracing reveals tissue metabolic activity. *Nat. Methods* **19**, 223–230 (2022).
28. Schuijs, M. J. et al. ILC2-driven innate immune checkpoint mechanism antagonizes NK cell antimetastatic function in the lung. *Nat. Immunol.* **21**, 998–1009 (2020).
29. Lam, K. H. B. et al. Topographic mapping of the glioblastoma proteome reveals a triple-axis model of intra-tumoral heterogeneity. *Nat. Commun.* **13**, 116 (2022).
30. Puchalski, R. B. et al. An anatomic transcriptional atlas of human glioblastoma. *Science* **360**, 660–663 (2018).
31. Kumar, S. et al. Intra-tumoral metabolic zonation and resultant phenotypic diversification are dictated by blood vessel proximity. *Cell Metab.* **30**, 201–211.e6 (2019).
32. Schwaiger-Haber, M. et al. Using mass spectrometry imaging to map fluxes quantitatively in the tumor ecosystem. *Nat. Commun.* **14**, 2876 (2023).
33. Hensley, C. T. et al. Metabolic heterogeneity in human lung tumors. *Cell* **164**, 681–694 (2016).
34. Daemen, A. et al. Metabolite profiling stratifies pancreatic ductal adenocarcinomas into subtypes with distinct sensitivities to metabolic inhibitors. *Proc. Natl Acad. Sci. USA* **112**, E4410–E4417 (2015).
35. King, R. J., Qiu, F., Yu, F. & Singh, P. K. Metabolic and immunological subtypes of esophageal cancer reveal potential therapeutic opportunities. *Front. Cell Dev. Biol.* **9**, 667852 (2021).
36. Mossa, F. et al. Subtype and site specific-induced metabolic vulnerabilities in prostate cancer. *Mol. Cancer Res.* **21**, 51–61 (2023).
37. Gentric, G. et al. PML-regulated mitochondrial metabolism enhances chemosensitivity in human ovarian cancers. *Cell Metab.* **29**, 156–173.e10 (2019).
38. Caro, P. et al. Metabolic signatures uncover distinct targets in molecular subsets of diffuse large B cell lymphoma. *Cancer Cell* **22**, 547–560 (2012).
39. Fala, M. et al. The role of branched-chain aminotransferase 1 in driving glioblastoma cell proliferation and invasion varies with tumor subtype. *Neurooncol. Adv.* **5**, vdad120 (2023).
40. Kurhanewicz, J. et al. Hyperpolarized ¹³C MRI: path to clinical translation in oncology. *Neoplasia* **21**, 1–16 (2019).
41. De Feyter, H. M. et al. Deuterium metabolic imaging (DMI) for MRI-based 3D mapping of metabolism in vivo. *Sci. Adv.* **4**, eaat7314 (2018).
42. Faubert, B., Tasdogan, A., Morrison, S. J., Mathews, T. P. & DeBerardinis, R. J. Stable isotope tracing to assess tumor metabolism in vivo. *Nat. Protoc.* **16**, 5123–5145 (2021).
43. Livermore, L. J., Ma, R., Bojanic, S. & Pereira, E. A. Yield and complications of frame-based and frameless stereotactic brain biopsy—the value of intra-operative histological analysis. *Br. J. Neurosurg.* **28**, 637–644 (2014).
44. Harrisson, S. E., Shooman, D. & Grundy, P. L. A prospective study of the safety and efficacy of frameless, pinless electromagnetic image-guided biopsy of cerebral lesions. *Neurosurgery* **70**, 29–33 (2012).
45. Dammers, R. et al. Towards improving the safety and diagnostic yield of stereotactic biopsy in a single centre. *Acta Neurochir. (Wien.)* **152**, 1915–1921 (2010).
46. Dannhorn, A. et al. Universal sample preparation unlocking multimodal molecular tissue imaging. *Anal. Chem.* **92**, 11080–11088 (2020).
47. Adusumilli, R. & Mallick, P. Data conversion with ProteoWizard msConvert. *Methods Mol. Biol.* **1550**, 339–368 (2017).
48. Race, A. M., Styles, I. B. & Bunch, J. Inclusive sharing of mass spectrometry imaging data requires a converter for all. *J. Proteom.* **75**, 5111–5112 (2012).
49. McAbee, J. H. et al. Detection of glioblastoma intratumor heterogeneity in radiosensitivity using patient-derived neurosphere cultures. *J. Neurooncol.* **149**, 383–390 (2020).
50. Kenney-Herbert, E. M., Ball, S. L., Al-Mayhani, T. M. & Watts, C. Glioblastoma cell lines derived under serum-free conditions can be used as an in vitro model system to evaluate therapeutic response. *Cancer Lett.* **305**, 50–57 (2011).
51. Bolger, A. M., Lohse, M. & Usadel, B. Trimmomatic: a flexible trimmer for Illumina sequence data. *Bioinformatics* **30**, 2114–2120 (2014).
52. Dobin, A. et al. STAR: ultrafast universal RNA-seq aligner. *Bioinformatics* **29**, 15–21 (2013).
53. Love, M. I., Huber, W. & Anders, S. Moderated estimation of fold change and dispersion for RNA-seq data with DESeq2. *Genome Biol.* **15**, 550 (2014).
54. Benjamini, Y. & Hochberg, Y. Controlling the false discovery rate: a practical and powerful approach to multiple testing. *J. R. Stat. Soc. Series B Stat. Methodol.* **57**, 289–300 (1995).
55. Wu, T. et al. clusterProfiler 4.0: a universal enrichment tool for interpreting omics data. *Innovation (Camb.)* **2**, 100141 (2021).
56. Marin-Valencia, I. et al. Analysis of tumor metabolism reveals mitochondrial glucose oxidation in genetically diverse human glioblastomas in the mouse brain in vivo. *Cell Metab.* **15**, 827–837 (2012).
57. Satija, R., Farrell, J. A., Gennert, D., Schier, A. F. & Regev, A. Spatial reconstruction of single-cell gene expression data. *Nat. Biotechnol.* **33**, 495–502 (2015).
58. Andreatta, M. & Carmona, S. J. UCell: robust and scalable single-cell gene signature scoring. *Comput. Struct. Biotechnol. J.* **19**, 3796–3798 (2021).

59. Cable, D. M. et al. Robust decomposition of cell type mixtures in spatial transcriptomics. *Nat. Biotechnol.* **40**, 517–526 (2022).
60. Darmanis, S. et al. Single-cell RNA-seq analysis of infiltrating neoplastic cells at the migrating front of human glioblastoma. *Cell Rep.* **21**, 1399–1410 (2017).

Acknowledgements

We are grateful to the CRUK Cambridge Institute Histology Core, Biological Resource Unit and Research and Instrumentation Core for technical support and to the members of the Brindle lab for discussions. We thank H. Bulstrode (Cambridge Stem Cell Institute) and previous members of C. Watts' lab for providing us with primary GB cell lines. A.T. was supported by the CRUK Rosetta Grand Challenge grant (A25045). O.A.B.'s work was supported by Wellcome Leap as part of the Delta Tissue programme. Work in K.M.B.'s lab is funded by CRUK grants (C197/A29580, C197/A17242, C9685/A25177).

Author contributions

A.T., A.D., G.H., M.P., D.-L.C., A.S., A.J.W. and R.M. performed data analysis and contributed to paper writing and editing. A.T., A.D., G.H., M.B., L.M., J.L.M., G.D.J., T.G., F.M., O.A.B., R.A., J.R. and R.M. were involved with data acquisition. C.B., L.M., E.C.W., L.F., G.D.J., T.G., F.M., O.A.B., J.R. and A.G.-F. performed data analysis. J.B., Z.T. and K.M.B. acquired funding. J.B., S.T.B., R.J.A.G. and K.M.B. were involved with project administration; R.A., R.M. and K.M.B. supervised the project. K.M.B. conceived the project and contributed to paper writing and editing; all authors reviewed the paper.

Competing interests

The authors declare no competing interests.

Additional information

Extended data is available for this paper at <https://doi.org/10.1038/s42255-025-01293-y>.

Supplementary information The online version contains supplementary material available at <https://doi.org/10.1038/s42255-025-01293-y>.

Correspondence and requests for materials should be addressed to Richard Mair or Kevin M. Brindle.

Peer review information *Nature Metabolism* thanks Leila Akkari, Shawn Davidson and the other, anonymous, reviewer(s) for their contribution to the peer review of this work. Primary Handling Editor: Alfredo Giménez-Cassina, in collaboration with the *Nature Metabolism* team.

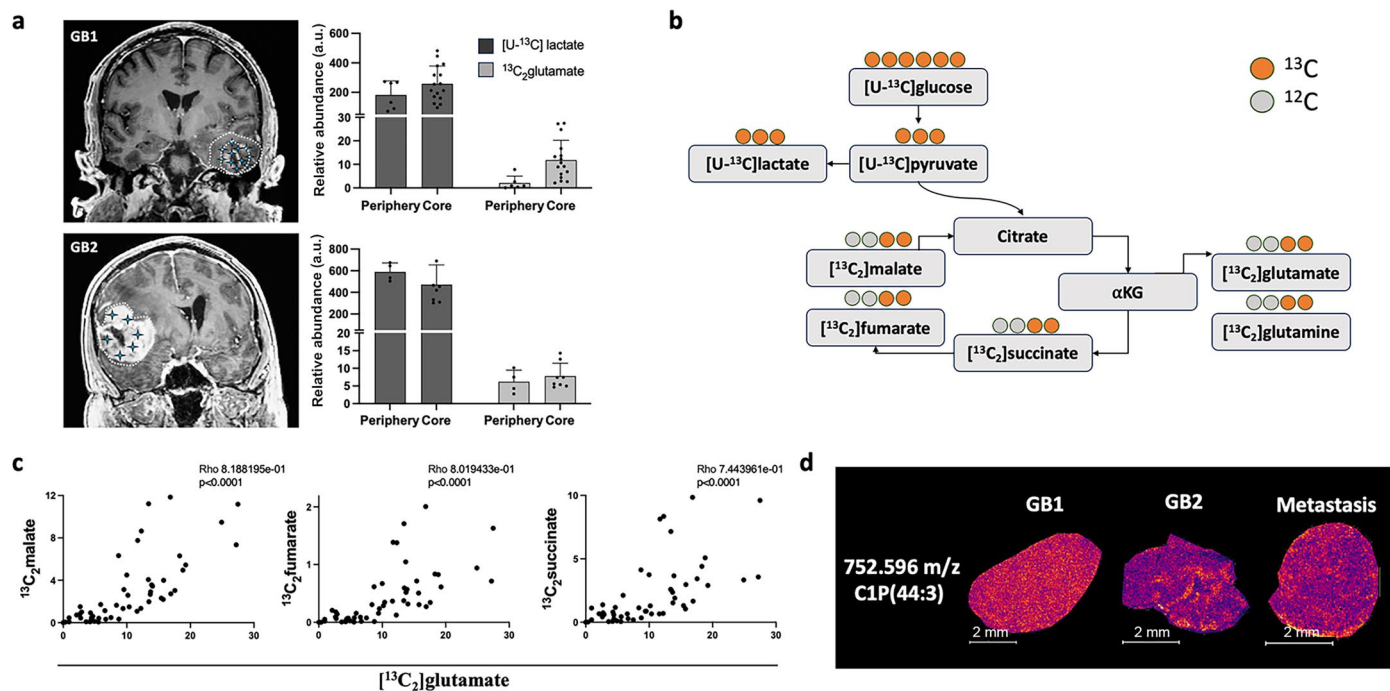
Reprints and permissions information is available at www.nature.com/reprints.

Publisher's note Springer Nature remains neutral with regard to jurisdictional claims in published maps and institutional affiliations.

Open Access This article is licensed under a Creative Commons Attribution 4.0 International License, which permits use, sharing, adaptation, distribution and reproduction in any medium or format, as long as you give appropriate credit to the original author(s) and the source, provide a link to the Creative Commons licence, and indicate if changes were made. The images or other third party material in this article are included in the article's Creative Commons licence, unless indicated otherwise in a credit line to the material. If material is not included in the article's Creative Commons licence and your intended use is not permitted by statutory regulation or exceeds the permitted use, you will need to obtain permission directly from the copyright holder. To view a copy of this licence, visit <http://creativecommons.org/licenses/by/4.0/>.

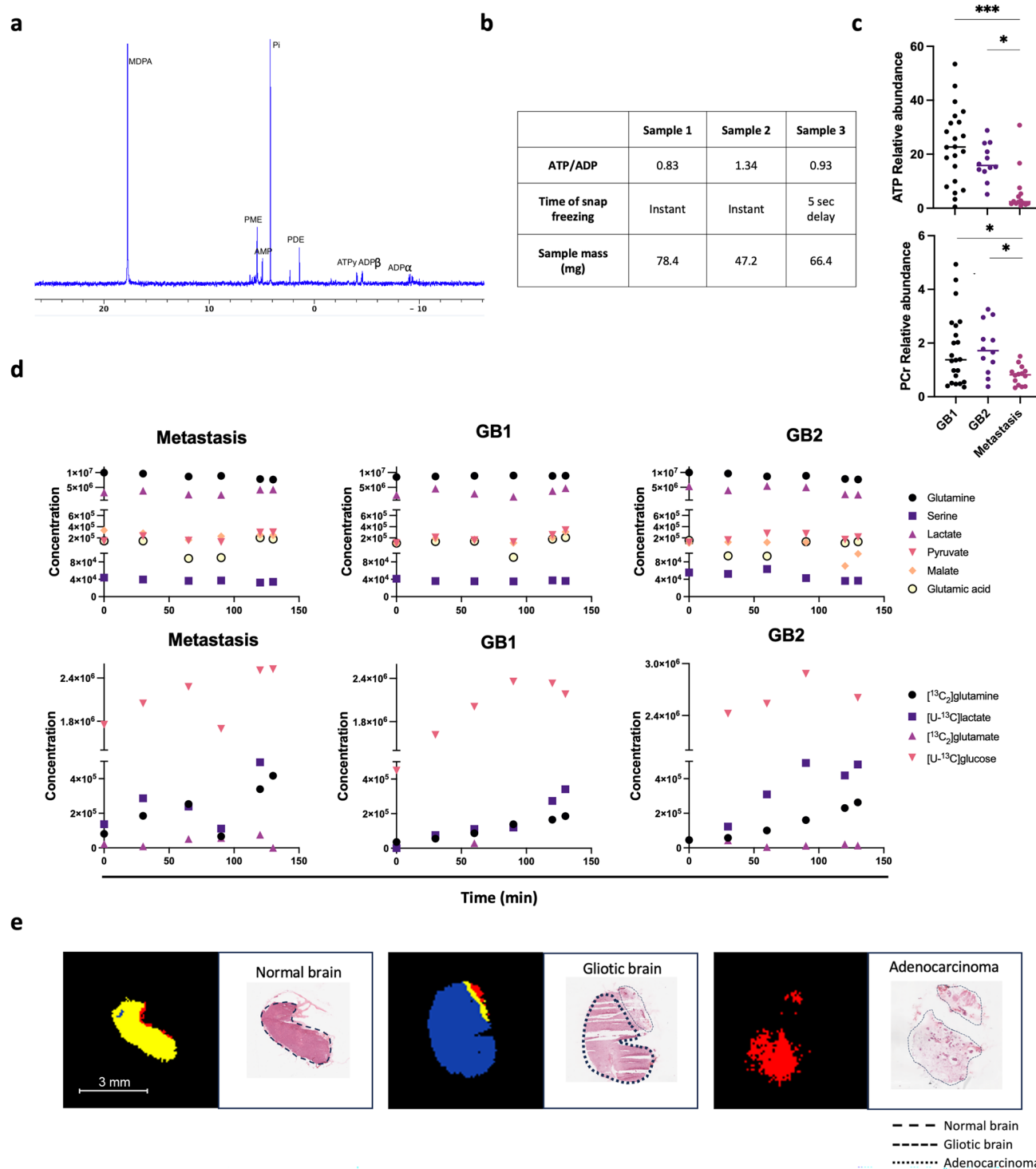
© The Author(s) 2025

¹Cancer Research UK Cambridge Institute, University of Cambridge, Cambridge, UK. ²Integrated BioAnalysis, Clinical Pharmacology & Safety Sciences R&D, AstraZeneca, Cambridge, UK. ³AstraZeneca, Cambridge Biomedical Campus, Cambridge, UK. ⁴Cambridge Stem Cell Institute, University of Cambridge, Cambridge, UK. ⁵Safety Sciences, Clinical Pharmacology & Safety Sciences R&D, AstraZeneca, Gothenburg, Sweden. ⁶Department of Gene Technology, KTH Royal Institute of Technology, Science for Life Laboratory, Stockholm, Sweden. ⁷Wellcome Sanger Institute, Wellcome Genome Campus, Hinxton, Cambridge, UK. ⁸National Physical Laboratory, Teddington, UK. ⁹Department of Metabolism, Digestion and Reproduction, Imperial College, London, UK. ¹⁰Department of Clinical Neurosciences, Cambridge Biomedical Campus, Cambridge, UK. ¹¹Department of Biochemistry, University of Cambridge, Cambridge, UK. *A full list of members and their affiliations appears in Supplementary Information. ✉e-mail: Richard.Mair@cruk.cam.ac.uk; kmb1001@cam.ac.uk



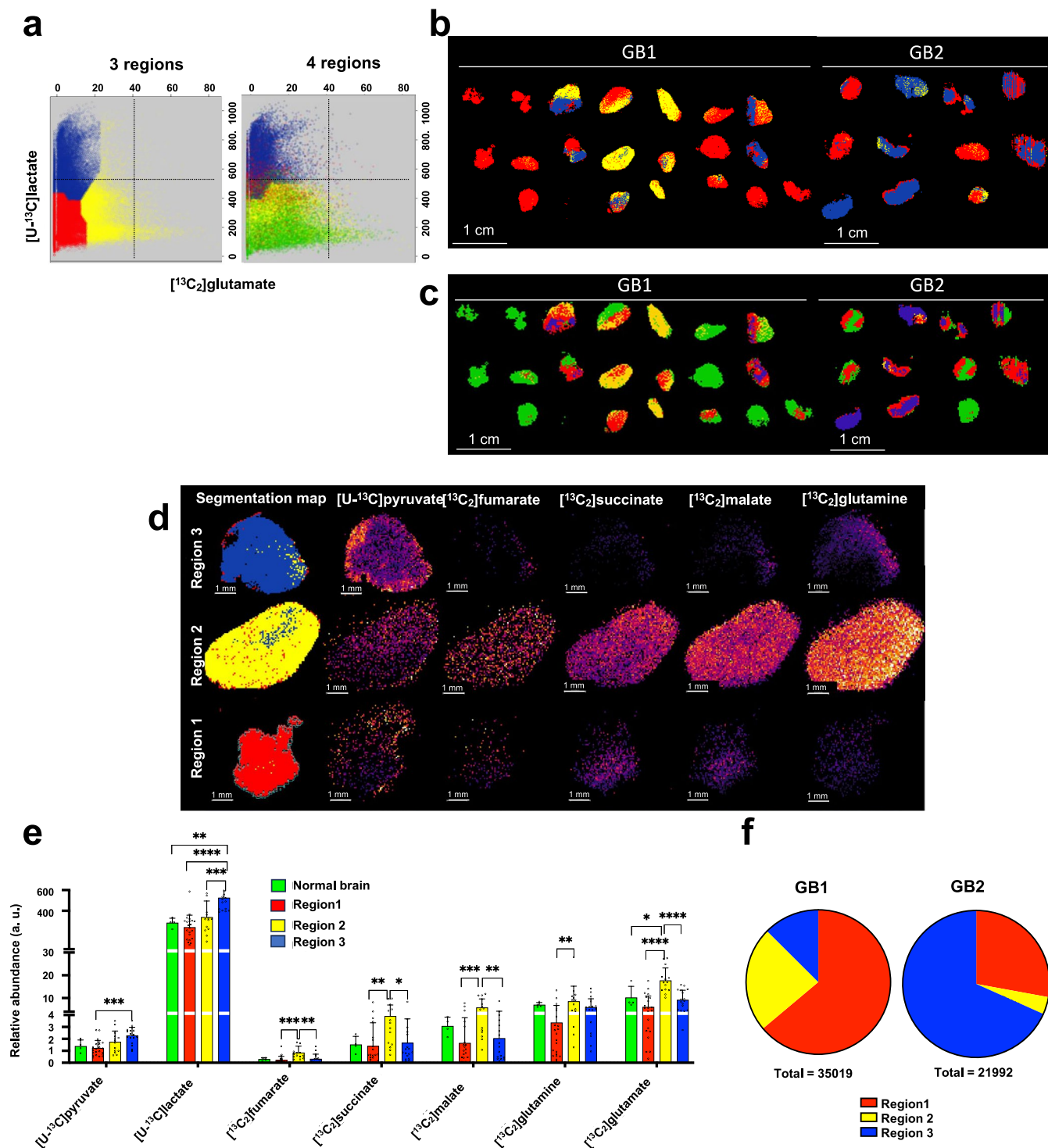
Extended Data Fig. 1 | Analysis of lactate and glutamate labelling in GB1 and GB2. **a** Coronal MR images from the two infused GB patients showing the locations of the sampled regions (blue stars). There were no significant differences in the mean signal intensities (\pm SD) of $[^{13}\text{C}_2]$ glutamate and $[\text{U-}^{13}\text{C}]$ lactate in the core and periphery of GB1 (core=9; periphery=13) and GB2 (core=8; periphery=4) (unpaired T-test). **b** Labelling of lactate and TCA cycle intermediates from $[\text{U-}^{13}\text{C}]$ glucose. **c** Simple linear regression of the $[^{13}\text{C}_2]$ glutamate signal intensities against the intensities of labelled TCA cycle

metabolites. Each dot represents the mean intensity of the metabolite per tumour section ($^{13}\text{C}_2$ malate: $R^2 = .55$, $F(1, 51) = 62.56$, $p < 0.0001$; $^{13}\text{C}_2$ fumarate: $R^2 = .45$, $F(1, 51) = 41.51$, $p < 0.0001$; $^{13}\text{C}_2$ succinate: $R^2 = .39$, $F(1, 51) = 32.05$, $p < 0.0001$) **d** MALDI-MSI images of C1P(44:3) intensity across the three different patient tumours. The first section from GB1 was located at the beginning of the slide and was imaged first while the last metastasis section was located at the end of the slide and was imaged last. Tumour section locations on the slides were randomised.



Extended Data Fig. 2 | Assessment of tumour bioenergetics and analysis of plasma metabolites. a) ^{31}P NMR spectrum of a patient's tumour extract. The sample was collected using pituitary rongeur followed by rapid intra-operative snap freezing. **b)** ATP/ADP ratios determined from ^{31}P NMR measurements on extracts from three patients tumours. The samples were frozen immediately or with 5 second delay. **c)** Relative ATP (GB1 vs met $p = 0.0001$; GB2 vs met $p = 0.0329$) and PCr (GB1 vs met $p = 0.0253$; GB2 vs met $p = 0.047$) signal intensities in each tumour section. Asterisks refer to P values obtained from a

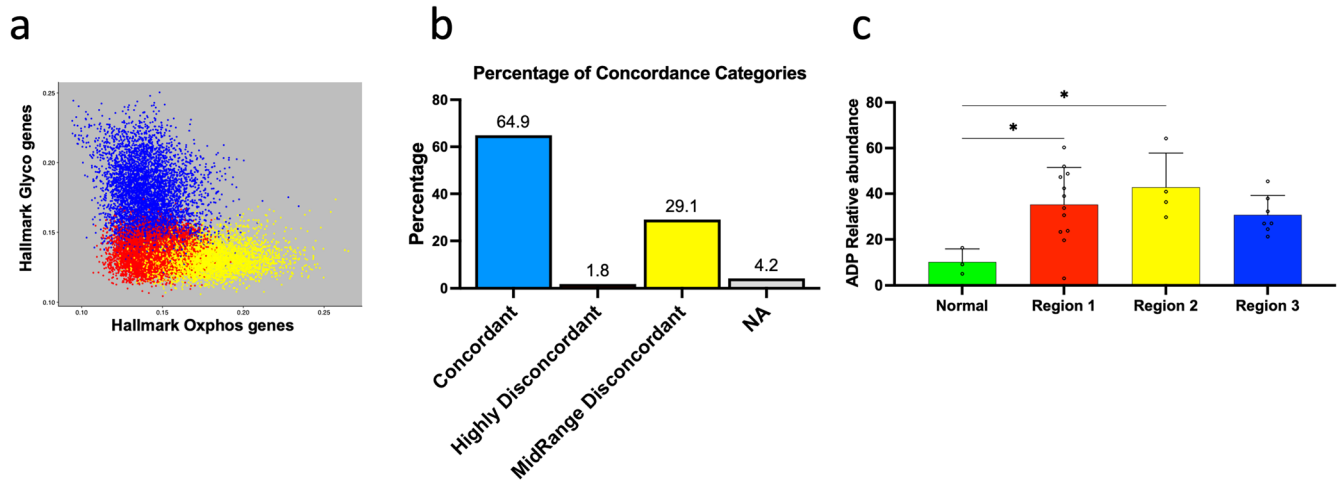
one way ANOVA test followed by Tukey's multiple comparisons test. **d)** Arterial blood concentrations of unlabelled (top) and labelled (bottom) metabolites, measured using LC-MS, in the three patients during $[\text{U-}^{13}\text{C}]$ glucose infusion. **e)** K-means segmentation, based on lactate and glutamate ^{13}C -labelling, of the adenocarcinoma metastasis into tumour (red), gliotic brain (blue), and normal brain (yellow). Corresponding H&E sections are shown (acquired post-DESI-MSI). Adenocarcinoma, gliotic brain and normal cortex are outlined. The H&E sections were annotated by a neuro histopathologist.



Extended Data Fig. 3 | Segmentation of the mass spectrometry images.

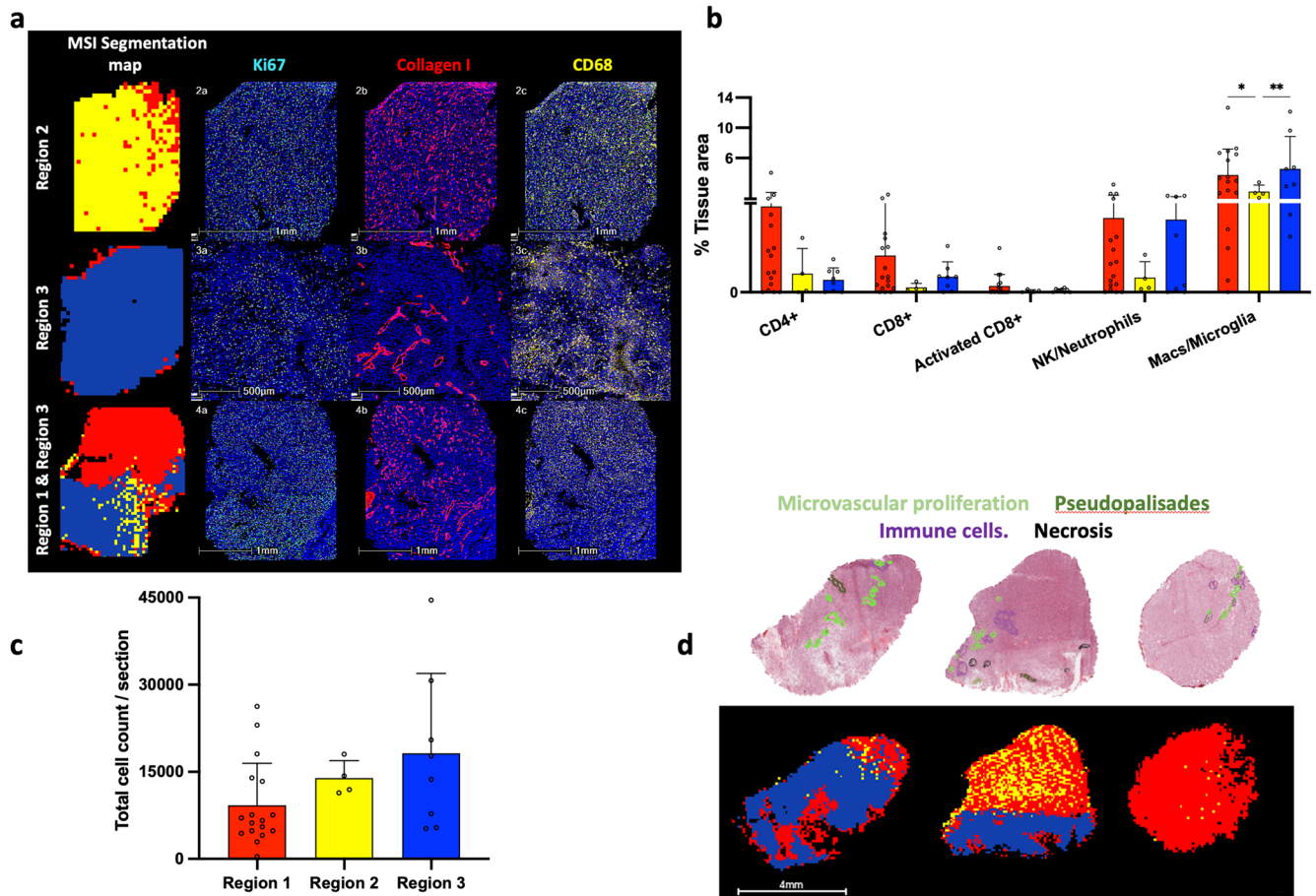
a) Scatter plot of individual pixel intensities in mass spectrometry images of tumour sections from GB1 and GB2. The x-axis shows $[^{13}\text{C}_2]\text{glutamate}$ and the y-axis shows $[\text{U-}^{13}\text{C}]\text{lactate}$ signal intensities. Colours correspond to the k-means segmentation of pixels into three vs. four groups. **b**) K-means segmentation maps of all the GB1 and GB2 tumour sections assuming three metabolic states. The three metabolic states are represented in red (low activity in glycolysis and TCA cycle), yellow (high TCA cycle activity) and blue (high glycolytic activity). The sections were arranged randomly on the slides for data acquisition. They have been arranged here to match their respective parent tumour in order to assist visualisation. **c**) K-means segmentation maps of all the GB1 and GB2

tumour sections assuming four metabolic states shown in **a**. **d**) Representative GB sections showing the three metabolic states and corresponding signal for ^{13}C labelled metabolites in glycolysis and the TCA cycle. **e**) Relative abundance of TCA cycle and glycolytic intermediates in the 3 metabolic states in GB1, GB2 and normal appearing brain ($n = 4$; Region 1 $n = 22$; Region 2 $n = 14$; Region 3 $n = 17$) expressed as mean \pm SD. **f**) GB1 had a higher proportion of oxidative regions in the tumor sections (Region 2, yellow) while GB2 had more glycolytic regions (Region 3, blue). The three metabolic phenotypes were present in both patients. Asterisks refer to P values obtained from one-way ANOVA test followed by Tukey's multiple comparisons test or unpaired T-test ($*P < 0.05$; $**P < 0.005$; $***P < 0.0005$; $****P < 0.00005$).



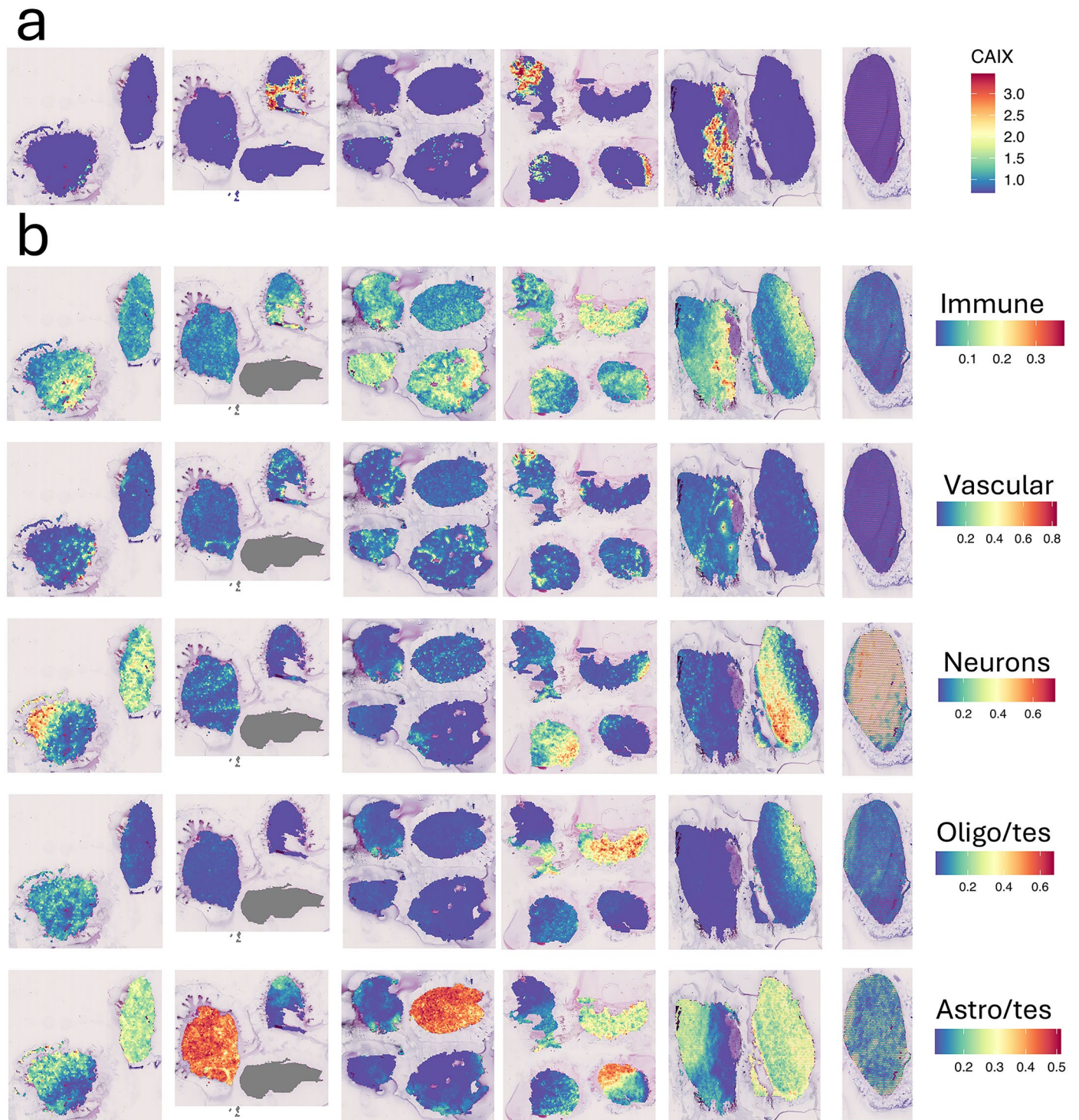
Extended Data Fig. 4 | Correlation between the mass spectrometry images and spatial transcriptomics. **a)** Spatial transcriptomic images were segmented using k-means into three metabolic groups, with blue representing highly glycolytic cells (expressing Hallmark glycolytic gene sets), yellow representing oxidative cells (expressing Hallmark oxidative gene sets) and red representing cells low for both glycolysis and oxidative phosphorylation transcripts.

b) Percent concordance between MSI and RNA derived metabolic states for all tumour pixels. **c)** ADP signal intensities (mean \pm SD) were significantly higher in the oxidative regions of GB defined by the MSI data (Normal $n = 3$; Region 1 $n = 12$; Region 2 $n = 4$; Region 3 $n = 7$). Asterisks refer to P values obtained from one way ANOVA test followed by Tukey's multiple comparisons test (* $P < 0.05$; ** $P < 0.005$; *** $P < 0.0005$; **** $P < 0.00005$).



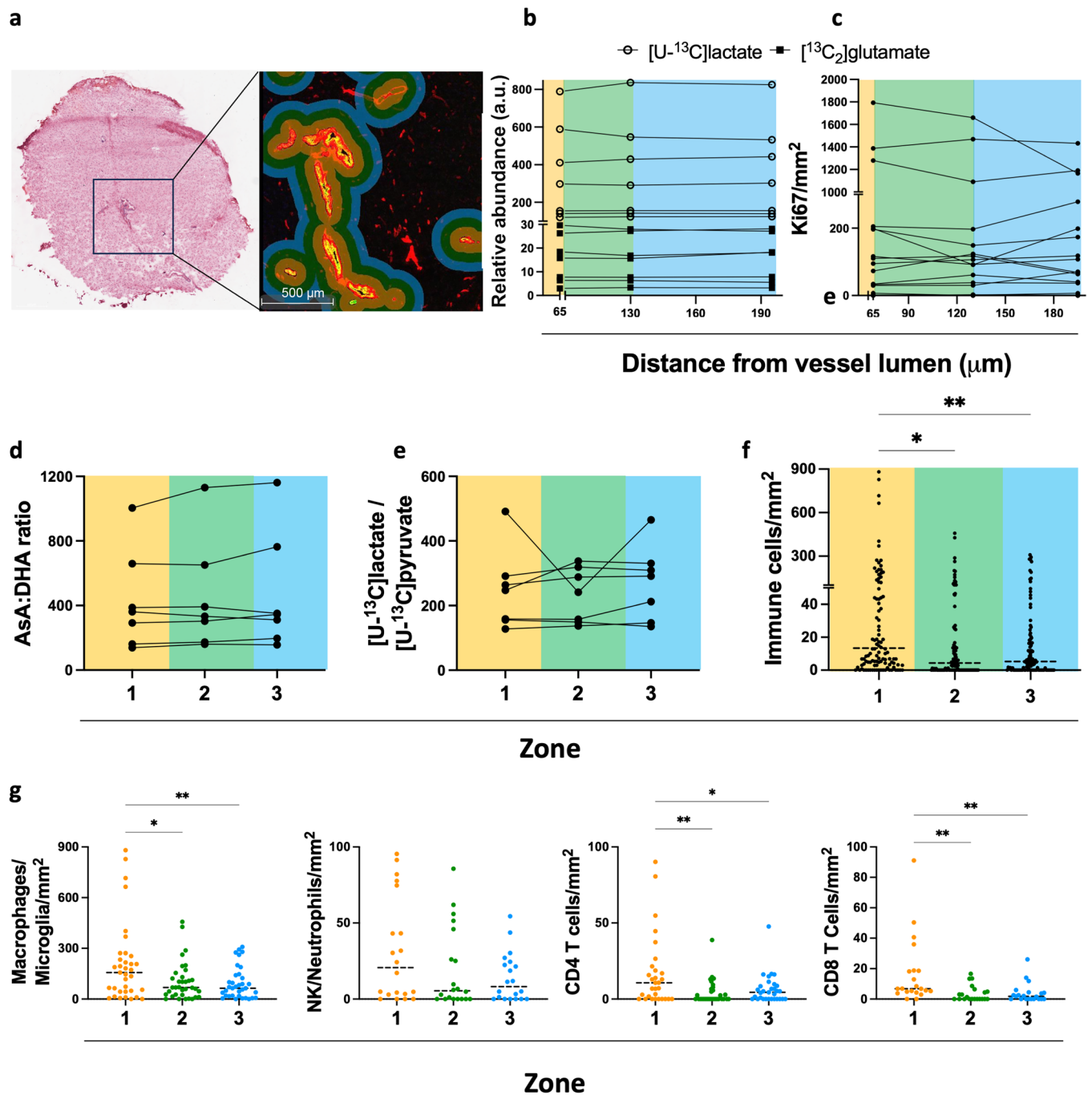
Extended Data Fig. 5 | Metabolic phenotypes are not affected by the tumour microenvironment. a Representative IHC images of Ki-67, Collagen I (large vessels), and CD68 (macrophages/microglia) positive cells in regions occupied by cells in one of the three metabolic states in GB tumours. **b** Quantification of specific immune cells in the regions occupied by one of the three tumour cell metabolic states using IHC (Region 1 n = 17; Region 2 n = 4; Region 3 n = 8; bar is mean \pm SD). **c** Total number of cells quantified using a DNA marker in the

metabolically defined regions (Region 1 n = 17; Region 2 n = 4; Region 3 n = 8; bar is mean \pm SD). **d** Representative H&E-stained sections were annotated by a histopathologist for the presence of necrosis, pseudopalisading necrosis, immune cells and microvascular proliferation. The segmented MS images shown below the H&E-stained sections demonstrate a lack of correlation between histological features and metabolic phenotype.



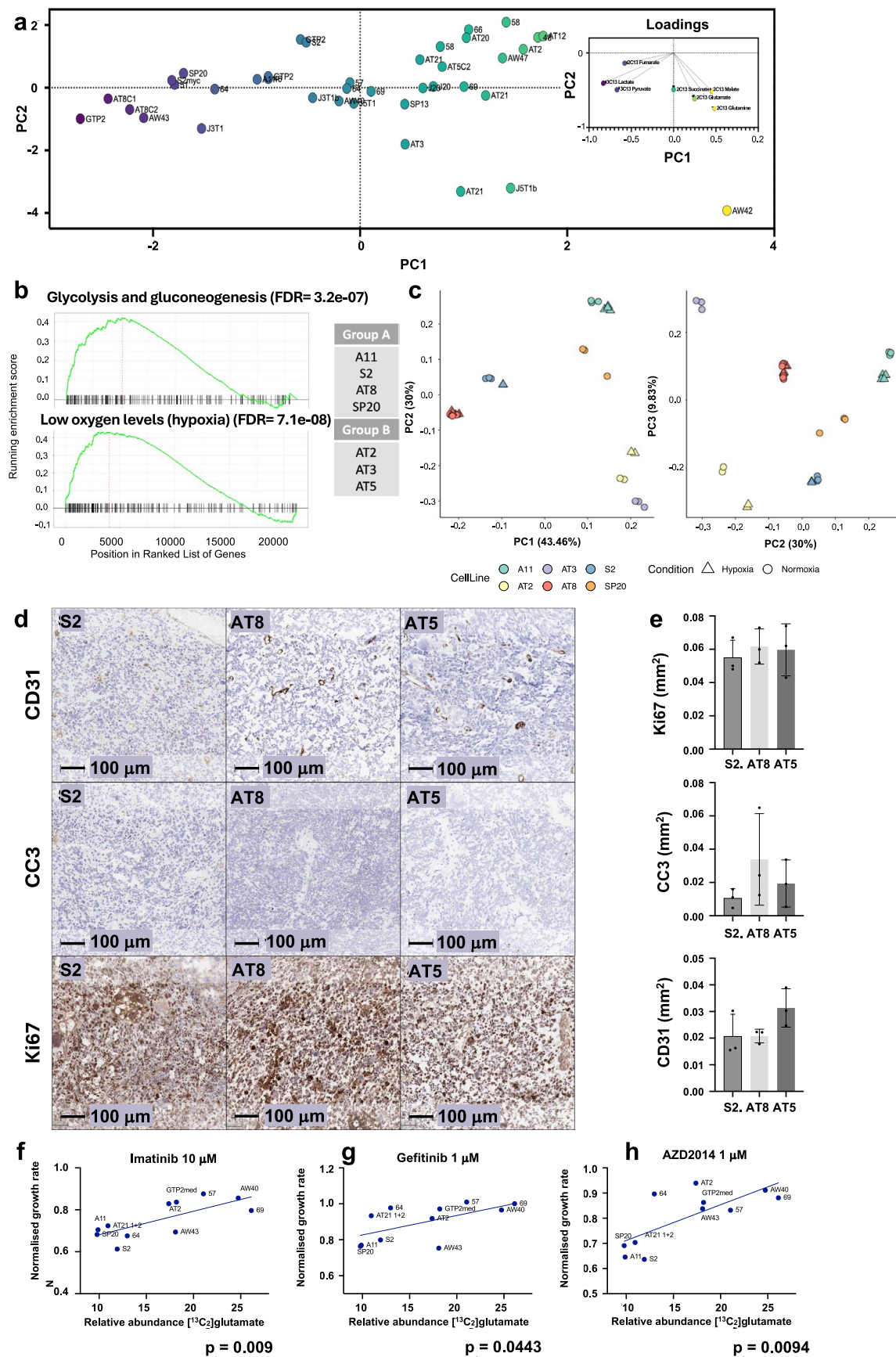
Extended Data Fig. 6 | Spatial transcriptomics showed similar numbers of microenvironmental cells in tumour regions occupied by the different metabolic states. a) Spatial expression of carbonic anhydrase IX (CAIX). b) Spatial distribution of RNA expression profiles for immune, vascular, neuron,

oligodendrocyte and astrocyte cell populations. Colours indicate the normalised weights and represent the percentage of the deconvolved population present per spot.



Extended Data Fig. 7 | Proximity to the vasculature has no effect on lactate and glutamate labelling. **a** *Left*: Representative H&E-stained GB section and (*right*) IMC of a contiguous section with double positive *Collagen I*⁺ and *αSMA* vessels. Three infiltration bands (yellow, green, blue), 65 μm wide, radiating from the vessel wall are shown. **b** Relative abundance of [U-¹³C]lactate and [¹³C₂]glutamate at the specified distances from the vessel wall. The colours correspond to the bands shown around each vessel in **a**. **c** Number of Ki67 positive nuclei/mm² in each infiltration band. The colours correspond to the infiltration bands around each vessel in **a**. **d** AsA:DHA and **e**) [U-¹³C]lactate/[U-¹³C]pyruvate ratios at 65 μm,

130 μm and 195 μm from the vessel wall. **f**) Total number of immune cells (n = 118 infiltration bands) and **g**) the number of specified immune cell subtypes within each infiltration band (Macs/microglia bands n = 35; NK/neutrophil bands n = 20; CD4⁺ n = 31; CD8⁺ n = 21). There were significantly more immune cells in the band closest to the vessel. Data are mean ± SD, where every dot is a tumour section or a region of a tumour section identified by k-means segmentation. Asterisks refer to *P* values obtained from one-way ANOVA test followed by Tukey's multiple comparisons test or unpaired T-test (**P* < 0.05; ***P* < 0.005).



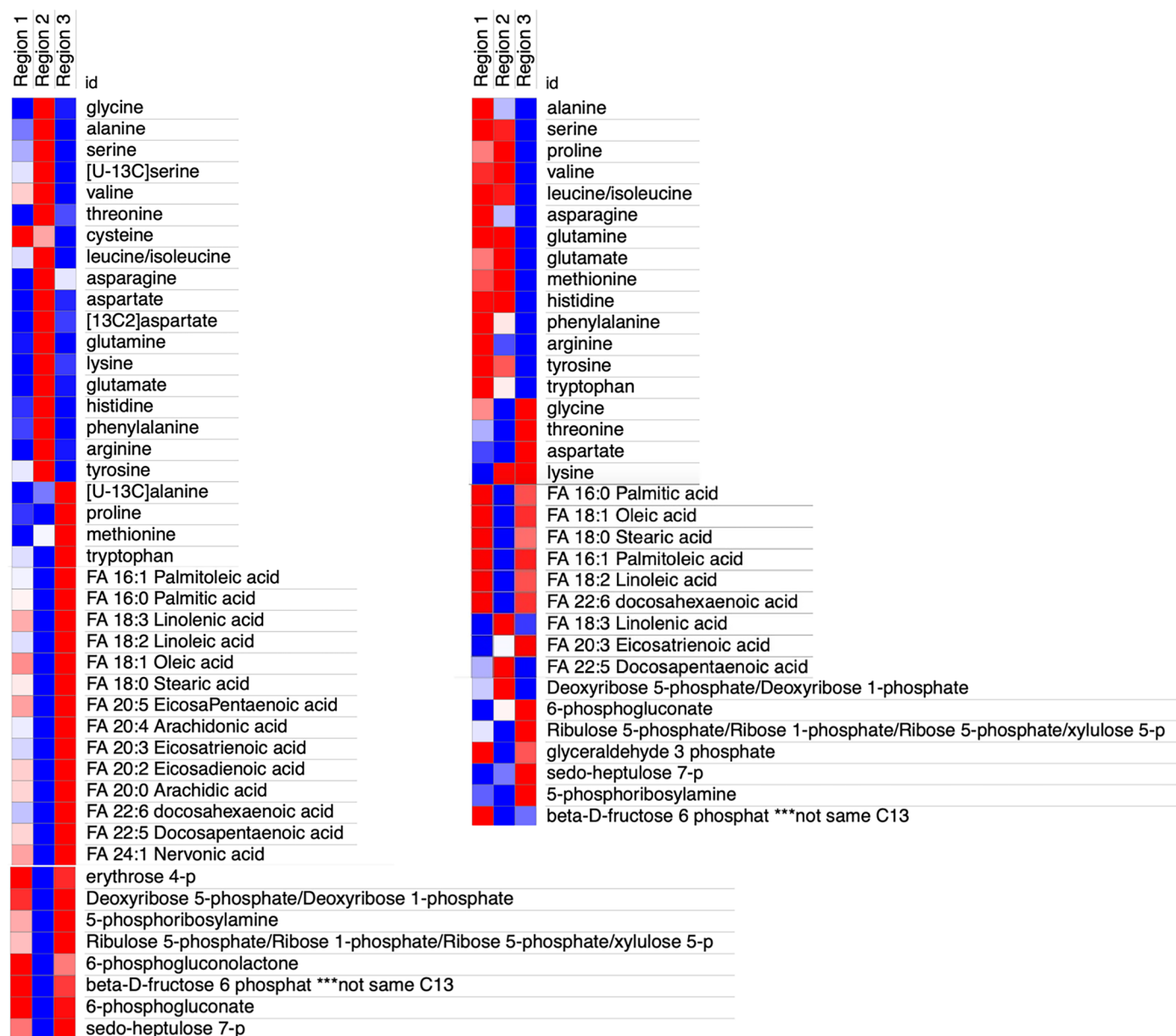
Extended Data Fig. 8 | See next page for caption.

Extended Data Fig. 8 | Characterisation of neurosphere and xenograft metabolic phenotypes. **a)** PCA plot using MSI signal intensities of ^{13}C -labelled pyruvate, lactate, succinate, malate, fumarate, glutamate and glutamine. The loadings plot (inset) shows that the oxidative spheres separate to the right of PC1 and the glycolytic spheres to the left. Although the MSI data were segmented into 3 metabolic phenotypes, the relative activities of the glycolytic and oxidative pathways are a continuum. **b)** Neurosphere RNA sequencing DGSEA analysis showed upregulation of hallmark genes in glycolysis and hypoxia in the more glycolytic spheres, as determined by MSI (labelled here as group A). **c)** Neurospheres grown in normoxia and hypoxia (0.5% O_2). PCA plot of RNA sequencing data showing separation of neurospheres into three groups.

Hypoxia did not shift the position of these groups on PC1 and PC2 significantly. **d)** Contiguous sections from S2, AT8 and AT5 xenografts stained for Ki-67, CC3 and CD31. **e)** Ki67, CC3 and CD31 signals normalized to tissue area (mm^2) were not significantly different between the three tumour models ($n = 3$ biological replicates per tumour model; data presented as mean \pm SD). **f, g, h)** Correlation of glutamate labelling in the primary cell lines with response to Imatinib ($R^2 = .55$, $F(1, 9) = 11.0$, $p = 0.009$) **(f)**, Gefitinib ($R^2 = .38$, $F(1, 9) = 5.46$, $p = 0.0443$) **(g)** and AZD2014 ($R^2 = .55$, $F(1, 9) = 10.83$, $p = 0.0094$) **(h)** treatment. The y-axis shows cell line response to drug normalised to control, where 1.0 indicates unsuppressed growth in the presence of the drug and values less than 1.0 indicate reduced cell growth relative to control.

Human Tumour

Neurospheres



Extended Data Fig. 9 | The metabolic phenotypes show signatures in other pathways. Concentrations of amino acids are higher in Region 2 (oxidative) in both human GB sections and neurospheres. The concentrations of fatty acids and PPP intermediates are higher in Region 1 and Region 3 (which are both more glycolytic than Region 2). There are fewer metabolites shown in the neurosphere

data because the DESI-Orbitrap data was acquired over a greater m/z range (70-1000 m/z) while the human data was acquired over a narrower range (70-280 m/z). This reduces the sensitivity of detection in neurospheres, particularly of the less abundant metabolites.

Reporting Summary

Nature Portfolio wishes to improve the reproducibility of the work that we publish. This form provides structure for consistency and transparency in reporting. For further information on Nature Portfolio policies, see our [Editorial Policies](#) and the [Editorial Policy Checklist](#).

Statistics

For all statistical analyses, confirm that the following items are present in the figure legend, table legend, main text, or Methods section.

- | n/a | Confirmed |
|-------------------------------------|--|
| <input type="checkbox"/> | <input checked="" type="checkbox"/> The exact sample size (n) for each experimental group/condition, given as a discrete number and unit of measurement |
| <input type="checkbox"/> | <input checked="" type="checkbox"/> A statement on whether measurements were taken from distinct samples or whether the same sample was measured repeatedly |
| <input type="checkbox"/> | <input checked="" type="checkbox"/> The statistical test(s) used AND whether they are one- or two-sided
<i>Only common tests should be described solely by name; describe more complex techniques in the Methods section.</i> |
| <input type="checkbox"/> | <input checked="" type="checkbox"/> A description of all covariates tested |
| <input type="checkbox"/> | <input checked="" type="checkbox"/> A description of any assumptions or corrections, such as tests of normality and adjustment for multiple comparisons |
| <input type="checkbox"/> | <input checked="" type="checkbox"/> A full description of the statistical parameters including central tendency (e.g. means) or other basic estimates (e.g. regression coefficient) AND variation (e.g. standard deviation) or associated estimates of uncertainty (e.g. confidence intervals) |
| <input type="checkbox"/> | <input checked="" type="checkbox"/> For null hypothesis testing, the test statistic (e.g. F , t , r) with confidence intervals, effect sizes, degrees of freedom and P value noted
<i>Give P values as exact values whenever suitable.</i> |
| <input checked="" type="checkbox"/> | <input type="checkbox"/> For Bayesian analysis, information on the choice of priors and Markov chain Monte Carlo settings |
| <input checked="" type="checkbox"/> | <input type="checkbox"/> For hierarchical and complex designs, identification of the appropriate level for tests and full reporting of outcomes |
| <input checked="" type="checkbox"/> | <input type="checkbox"/> Estimates of effect sizes (e.g. Cohen's d , Pearson's r), indicating how they were calculated |

Our web collection on [statistics for biologists](#) contains articles on many of the points above.

Software and code

Policy information about [availability of computer code](#)

Data collection

Data analysis

For manuscripts utilizing custom algorithms or software that are central to the research but not yet described in published literature, software must be made available to editors and reviewers. We strongly encourage code deposition in a community repository (e.g. GitHub). See the Nature Portfolio [guidelines for submitting code & software](#) for further information.

Data

Policy information about [availability of data](#)

All manuscripts must include a [data availability statement](#). This statement should provide the following information, where applicable:

- Accession codes, unique identifiers, or web links for publicly available datasets
- A description of any restrictions on data availability
- For clinical datasets or third party data, please ensure that the statement adheres to our [policy](#)

The non-human data generated for this study will be made publicly available in the University of Cambridge data repository (<https://www.repository.cam.ac.uk/home>). RNA neurosphere sequencing data is available under the following GEO accession number: GSE288836. R code for generating K means groups in human and sphere MSI data is available in the University of Cambridge data repository (<https://www.repository.cam.ac.uk/home>) under the file name: 2-20240214-FinalPlots.R. VISIUM spatial transcriptomics human R code and analysis is available in the University of Cambridge data repository (<https://www.repository.cam.ac.uk/home>) under the file name seurat_obj.R. Human data: The authors declare that the clinical and imaging data supporting the findings of this study are available within the article and its Supplementary Information. The authors defer raw DESI-MSI and clinical MRI data deposition to ensure compliance with legal requirements of the University of Cambridge and Cambridge University Hospitals NHS Foundation Trust and avoid breaching data sharing regulations for human participants. Requests for raw data can be referred to the corresponding author; these will be reviewed within ten working days in consultation with the institutional R&D which will determine the terms of a data transfer agreement between the recipient institution, the University of Cambridge, and Cambridge University Hospitals NHS Foundation Trust.

Research involving human participants, their data, or biological material

Policy information about studies with [human participants or human data](#). See also policy information about [sex, gender \(identity/presentation\), and sexual orientation](#) and [race, ethnicity and racism](#).

Reporting on sex and gender	Gender was not considered in the study design
Reporting on race, ethnicity, or other socially relevant groupings	No data on race or ethnicity was collected as part of the study design.
Population characteristics	No data on population characteristics was collected in this study.
Recruitment	Patient were recruited to the study following review by consultant Neurosurgeon in the outpatient setting. Only patients suitable, in terms of their general health and co-morbidities, to undergo tumour resection and general anaesthetic were recruited to the study. In addition, MRI was used to select patients with tumours amenable to surgical resection and intra-operative sampling (non-eloquent brain areas, minimal necrosis/cystic component).
Ethics oversight	The study was approved by East of England - Cambridge East Research Ethics Committee - REC 18/EE/0283. Protocol was approved by Cambridge University Hospitals, Addenbrooke's Hospital, Cambridge.

Note that full information on the approval of the study protocol must also be provided in the manuscript.

Field-specific reporting

Please select the one below that is the best fit for your research. If you are not sure, read the appropriate sections before making your selection.

- Life sciences Behavioural & social sciences Ecological, evolutionary & environmental sciences

For a reference copy of the document with all sections, see [nature.com/documents/nr-reporting-summary-flat.pdf](https://www.nature.com/documents/nr-reporting-summary-flat.pdf)

Life sciences study design

All studies must disclose on these points even when the disclosure is negative.

Sample size	Multiple samples were taken from 3 patients with brain tumours that had been infused with [U-13C]glucose. GB1, 40 samples from 10 different regions. GB2, 30 samples from 6 different regions. Metastasis patient, 30 samples from 7 different regions. The determination of sample number per patient were not-predetermined. Rather, the number was guided by intra-operative conditions and patient safety. E.g. localised bleeding following sample collection, time restraints to minimise general anaesthetic, proximity to eloquent brain areas. Thirty- cell lines, derived from 26 different patients, were analyzed as neurospheres. The number of cell lines derived was random.
Data exclusions	Nil
Replication	Several human GB tumour sections and slides were generated for the experiment. Because these were consecutive sections from a tumour, they could be classed as biological replicates. Two separate MSI runs were then performed on the consecutive sections to confirm the metabolic group presence across multiple batches. For the neurosphere experiment, each matrigel dome contained a single cell line with

multiple (>5) neurospheres from different passages and frozen vials. These therefore served as both technical and biological replicates. All in vitro work included 6 technical replicates and 3 biological replicates.

Randomization Samples were positioned randomly on slide for Mass Spectrometry Imaging. During analysis all samples were assigned random numbers so as not to bias analysis. There was no group allocation performed prior to analysis.

Blinding Data analysis was blinded to region of acquisition and patient sample. All GB sections were assigned a random number and processed and analysed in one batch.

Reporting for specific materials, systems and methods

We require information from authors about some types of materials, experimental systems and methods used in many studies. Here, indicate whether each material, system or method listed is relevant to your study. If you are not sure if a list item applies to your research, read the appropriate section before selecting a response.

Materials & experimental systems

n/a	Involvement in the study
<input type="checkbox"/>	<input checked="" type="checkbox"/> Antibodies
<input type="checkbox"/>	<input checked="" type="checkbox"/> Eukaryotic cell lines
<input checked="" type="checkbox"/>	<input type="checkbox"/> Palaeontology and archaeology
<input type="checkbox"/>	<input checked="" type="checkbox"/> Animals and other organisms
<input type="checkbox"/>	<input checked="" type="checkbox"/> Clinical data
<input checked="" type="checkbox"/>	<input type="checkbox"/> Dual use research of concern
<input checked="" type="checkbox"/>	<input type="checkbox"/> Plants

Methods

n/a	Involvement in the study
<input checked="" type="checkbox"/>	<input type="checkbox"/> ChIP-seq
<input checked="" type="checkbox"/>	<input type="checkbox"/> Flow cytometry
<input checked="" type="checkbox"/>	<input type="checkbox"/> MRI-based neuroimaging

Antibodies

Antibodies used

IMC antibodies:
 αSMA 141Pr 1A4 1:50 3141017D Standard Biotoools
 Vimentin 143Nd RV202 1:100 3143029D Standard Biotoools
 CD31 145Nd JC/70A 1:50 ab264090 Abcam
 Cleaved Caspase 3 147Sm E83-77 1:50 ab208003 Abcam
 Pan-CK 148Nd C11 1:50 3148020D Standard Biotoools
 CD45 152Sm D9M8I 1:100 3152018D Standard Biotoools
 CD3 154Sm UCHT1 1:50 3170022D Standard Biotoools
 CD4 156Gd RPA-T4 1:50 3156036D Standard Biotoools
 CD68 159Tb KP1 1:100 3159035D Standard Biotoools
 CD8 162Dy RPA-T8 1:50 3162036D Standard Biotoools
 Ki67 168 Er B56 1:50 3168022D Standard Biotoools
 Collagen I 169Tm Polyclonal 1:100 3169023D Standard Biotoools
 Granzyme B 167 ER GB11 1:50 3167023D Standard Biotoools
 p53 165 DO-7 1:50 MA5-12557 Thermo Fisher
 IHC antibodies:
 Ki67 Dako M7240 1:1000
 CC3 Cell Signaling Technology, 9664 1:250
 CD31 Abcam, ab182981, 1.128ug/ml

Validation

Validation was performed as per manufacturer's instructions available online. All antibodies were validated using positive (in tissue known to express high levels of protein of interest) and negative controls in normal and tumour tissue. The IHC antibodies were tested using a pre-determined Bond protocol, using both sodium citrate and Tris EDTA HIERS, no primary controls for each retrieval and a range of antibody dilutions. Custom IMC antibodies were tagged with lanthanides in house, using Fluidigm labeling kits, according to the manufacturer's instructions. All IMC antibodies were validated in house using conventional IHC as well as corresponding IMC staining and assessed by a pathologist.

Eukaryotic cell lines

Policy information about [cell lines and Sex and Gender in Research](#)

Cell line source(s)

Human-derived cell lines were sourced from the ICARUS biorepository (REC 18/EE/0172). The following primary human GB cell lines were used in the study: GTP2med, GTP2lat, AT8C1, AT8C2, AW43, AW40, AW42, J3T1, SP20, S2, S1, 64, A11, 57, 64, 69, J5T1, 58, 66, AT20, AT21ant, AT21post, AT5, J20, SP13, AT2, AT3, At12, 48, J5T2

Authentication

STR authentication.

Mycoplasma contamination

All cell lines tested negative for mycoplasma.

Commonly misidentified lines
(See [ICLAC](#) register)

None. All cell lines were primary human cell lines and were STR authenticated.

Animals and other research organisms

Policy information about [studies involving animals](#); [ARRIVE guidelines](#) recommended for reporting animal research, and [Sex and Gender in Research](#)

Laboratory animals	Female athymic RNU rats (Charles River). All animals were 6-8 weeks old at the time of tumour orthotopic implantation.
Wild animals	No wild animals were used in the study.
Reporting on sex	All athymic rats used in the study were female. Sex was not considered as part of the study design.
Field-collected samples	No field- collected samples were used in the study.
Ethics oversight	Procedures were performed in compliance with personal and project licenses issued under the United Kingdom Animals Scientific Procedures Act (1986) and approved by the Cancer Research UK, Cambridge Institute Animal Welfare, and Ethical Review Body.

Note that full information on the approval of the study protocol must also be provided in the manuscript.

Clinical data

Policy information about [clinical studies](#)

All manuscripts should comply with the ICMJE [guidelines for publication of clinical research](#) and a completed [CONSORT checklist](#) must be included with all submissions.

Clinical trial registration	REC 18/EE/0172 for cell lines, REC 18/EE/0283 for infusion studies
Study protocol	Three patients from Addenbrooke's Hospital, Cambridge, were infused with [U-13C] glucose. The selection criteria included first clinical presentation and MR images consistent with GB as well as no significant co-morbidities, particularly diabetes mellitus. On the day of the surgery, following induction of anaesthesia, a pyrogen free 5% solution of [U-13C]glucose in sterile saline (Merck, Frankfurter Strasse, Germany) was administered as bolus of 8 g over 10 minutes followed by 8 g/h continuous infusion, as described previously for GB patients and several other tumour types. Arterial blood was collected via a peripheral arterial line prior to bolus administration and then every 15 min following the start of infusion and at 15 min after the end of the infusion. Tumour sampling was guided by intra-operative Stealth navigation, and assessment of 5-ALA fluorescence. Tumours were sampled between 90-150 min as this had been shown previously to be the approximate time at which there was steady state 13C enrichment of plasma glucose. A pituitary rongeur was used to transfer tumour samples directly into liquid nitrogen (LN2). The freezing time was <5 seconds between tissue devascularisation and immersion in LN2.
Data collection	Data was collected via patients recruited at Addenbrooke's Hospital, Cambridge.
Outcomes	N/A

Plants

Seed stocks	NA
Novel plant genotypes	NA
Authentication	NA